drones

MDPI

Article

Comparing Unmanned Aerial Multispectral and Hyperspectral Imagery for Harmful Algal Bloom Monitoring in Artificial Ponds Used for Fish Farming

Diogo Olivetti [1,*], Rejane Cicerelli [1], Jean-Michel Martinez [1,2], Tati Almeida [1], Raphael Casari [1], Henrique Borges [1] and Henrique Roig [1]

[1] Campus Darcy Ribeiro, Institute of Geosciences, University of Brasília, ICC—Ala Central—CEP, Brasília 70910-900, Brazil
[2] Centre National de la Recherche Scientifique (CNRS), Géosciences Environnement Toulouse (GET), UMR5563, Institut de Recherche pour le Développement (IRD), Université Toulouse 3, 14 Avenue Edouard Belin, 31400 Toulouse, France
* Correspondence: olivetti.diogo@unb.br

Abstract: This work aimed to assess the potential of unmanned aerial vehicle (UAV) multi- and hyperspectral platforms to estimate chlorophyll-*a* (Chl-*a*) and cyanobacteria in experimental fishponds in Brazil. In addition to spectral resolutions, the tested platforms differ in the price, payload, imaging system, and processing. Hyperspectral airborne surveys were conducted using a push-broom system 276-band Headwall Nano-Hyperspec camera onboard a DJI Matrice 600 UAV. Multispectral airborne surveys were conducted using a global shutter-frame 4-band Parrot Sequoia camera onboard a DJI Phantom 4 UAV. Water quality field measurements were acquired using a portable fluorometer and laboratory analysis. The concentration ranged from 14.3 to 290.7 µg/L and from 0 to 112.5 µg/L for Chl-*a* and cyanobacteria, respectively. Forty-one Chl-*a* and cyanobacteria bio-optical retrieval models were tested. The UAV hyperspectral image achieved robust Chl-*a* and cyanobacteria assessments, with RMSE values of 32.8 and 12.1 µg/L, respectively. Multispectral images achieved Chl-*a* and cyanobacteria retrieval with RMSE values of 47.6 and 35.1 µg/L, respectively, efficiently mapping the broad Chl-*a* concentration classes. Hyperspectral platforms are ideal for the robust monitoring of Chl-*a* and CyanoHABs; however, the integrated platform has a high cost. More accessible multispectral platforms may represent a trade-off between the mapping efficiency and the deployment costs, provided that the multispectral cameras offer narrow spectral bands in the 660–690 nm and 700–730 nm ranges for Chl-*a* and in the 600–625 nm and 700–730 nm spectral ranges for cyanobacteria.

Keywords: inland water; remote sensing; UAV; remotely piloted aircraft (RPA); drone; Parrot Sequoia; Headwall Nano-Hyperspec; chlorophyll-*a*; cyanobacteria; CyanoHABs

Citation: Olivetti, D.; Cicerelli, R.; Martinez, J.-M.; Almeida, T.; Casari, R.; Borges, H.; Roig, H. Comparing Unmanned Aerial Multispectral and Hyperspectral Imagery for Harmful Algal Bloom Monitoring in Artificial Ponds Used for Fish Farming. *Drones* **2023**, *7*, 410. https://doi.org/10.3390/drones7070410

Academic Editors: Paschalis Koutalakis and Ourania Tzoraki

Received: 2 April 2023
Revised: 12 June 2023
Accepted: 13 June 2023
Published: 21 June 2023

1. Introduction

Phytoplankton are the most abundant primary producers in both inland and oceanic waters. Therefore, they play a significant role in global oxygen production and their monitoring is crucial for studies of the planet's biogeochemical cycles [1,2]. In inland waters, phytoplankton monitoring is essential for water use management, as it serves as an indicator of water trophic levels. Furthermore, the proliferation of cyanobacteria and other toxin-producing algae species (harmful algal blooms—HABs) can pose risks to aquatic biota and even public health [2,3].

Remote sensing techniques, particularly satellite imagery, have been widely applied to monitor phytoplankton and HABs in continental and oceanic waters using bio-optical models [4–8]. Chlorophyll-*a* (Chl-*a*) is a photosynthetically and optically active pigment, extensively used as an indicator of phytoplankton biomass in water quality monitoring employing remote sensing techniques [2]. For cyanobacteria estimation, phycocyanin (PC)

has been widely applied, as it is the only photosynthetic pigment intrinsically related to this type of phytoplankton [9].

Robust Chl-*a* and cyanobacteria monitoring in inland waters demands higher spectral resolutions than oceanic waters [10], corresponding to case II and case I waters, respectively [11]. In oceanic waters, Chl-*a* monitoring has been effectively applied using broadbands in blue and green wavelengths. However, this technique is less feasible in inland waters due to the significant influence of other optically active components (OACs), such as total suspended solids (TSS) and colored dissolved organic matter (CDOM), at these wavelengths. Consequently, narrow bands of intense Chl-*a* absorption at 660–680 nm and reflectance at 700–720 nm have been used with satisfactory results for monitoring this parameter in inland waters [4,12,13]. For cyanobacteria, the main spectral feature of PC is the absorption effect at 620–630 nm. Similar to Chl-*a*, bio-optical PC semi-empirical models have also been applied with narrow bands covering the absorption peak at 620–630 nm and the reflectance at 700–720 nm for PC at red wavelengths [9,14,15].

The recent and ongoing development of unmanned aerial vehicles (UAV) and small cameras has led to a new remote sensing platform capable of bridging the gaps between orbital and in situ platforms [16]. UAV platforms offer operational flexibility and the ability to record short- to long-term algal bloom events at the centimeter scale [17]. Numerous studies have demonstrated that UAV platforms can contribute valuable hydrology [18,19] and water quality information [20,21], regarding algae [17,22–24] and other optically active constituents [25–27]. The photogrammetry technique is widely employed in constructing orthomosaics for many of these applications. However, it has certain limitations when it comes to monitoring homogeneous areas, such as large bodies of water. To address this issue, alternative water mosaicking techniques and sun glint corrections have been developed as solutions [28,29].

UAV platforms offer not only ultra-high temporal and spatial resolution but also, depending on the camera carried, the capability to provide a high spectral resolution with suitable bands for robust phytoplankton monitoring. However, it is important to note that there is a diversity of optical system cameras available, which differ in terms of imaging systems, acquisition geometry, and spectral resolution [30], as well as weight, which may require drones with a higher payload capacity, consequently affecting the price and accessibility for projects or users with limited resources. High-cost hyperspectral cameras provide extremely narrow bands, capable of reproducing Chl-*a* and PC estimation algorithms developed from a field spectroradiometer. More affordable multispectral cameras are limited in reproducing these algorithms but can replicate other algorithms developed from multispectral satellite imagery and may even have bands that cover or approximate wavelengths of Chl-*a* and PC effects.

In this context, the objective of this study was to apply and evaluate the potential of Chl-*a* and cyanobacteria bio-optical models in fishponds using a 276-band hyperspectral camera and a 4-band multispectral camera, which also differ in the price, imaging system, payload, UAV platform, and image processing. Furthermore, this study aims to propose ideal bands for Chl-*a* and cyanobacteria monitoring with multispectral cameras.

2. Materials and Methods

2.1. Experimental Area and Water Quality Parameters

The experimental area is located in the center of Brazil (Figure 1B), within the *cerrado* (savanna) biome, near Brasília city (Figure 1C), the country's capital. The region's climate is tropical, characterized by a rainy season from October to March (spring–summer) and a dry period from April to September (autumn–winter). The annual average precipitation ranges from 1200 to 1800 mm, with January being the rainiest month (284 mm of precipitation) and June being the driest month (7 mm of precipitation, on average).

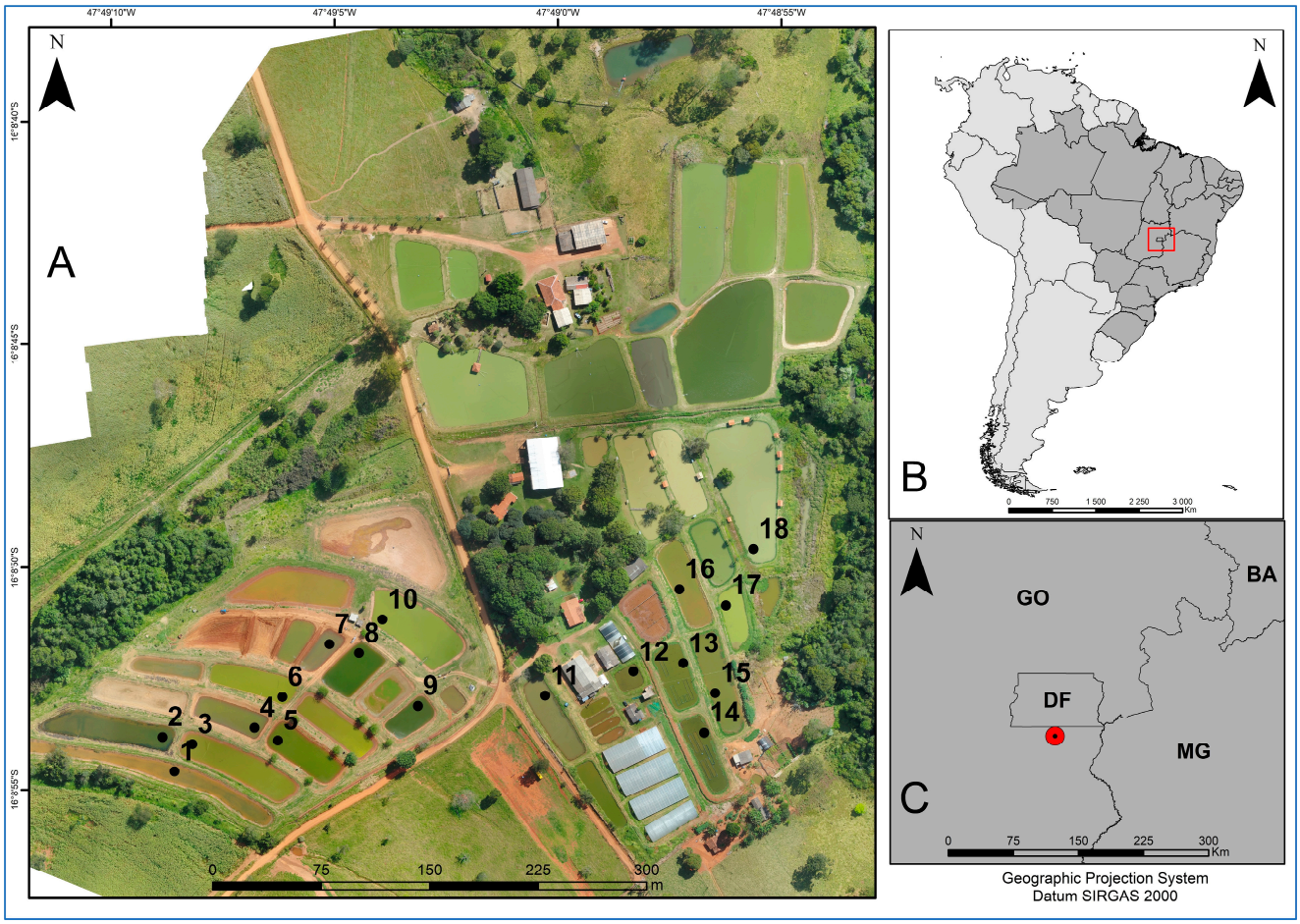

Figure 1. Location map of the ponds analyzed in this study, in the center of Brazil (**B**,**C**). Field sampling points numbered from 1 to 18 are displayed on a high-resolution image acquired by Phantom 4 during the UAV survey (**A**).

The study was conducted in fish farmland ponds used for fry breeding, where each pond exhibited a distinct water quality standard. Each pond has an area of approximately 1000 m^2 and is 1.6 m deep. Figure 1A displays the location map of these ponds in a high spatial resolution orthomosaic obtained from true-color red–blue–green (RGB) images captured by the UAV Phantom 4 system. The sampling points for in situ water quality data are also shown in the same figure.

Concurrently with the airborne multi- and hyper-spectral data acquisition, in situ water quality data were collected. Eighteen sampling locations were defined across the area, one for each pond. Water samples were collected at a depth of 15 cm between 10:00 am and 2:00 pm on 31 May 2019, using 1000 mL dark plastic bottles with a 1.5 m-long handle. The water samples were placed on ice immediately after collection and transported to the laboratory for processing. On the same day as the fieldwork, the water samples were filtered through a glass fiber filter with a pore size of 0.7 µm using a vacuum suction pump and a polysulfone filtration unit. The filtered samples were stored at a temperature below 0 °C and were subsequently diluted in acetone for stratification in a spectrophotometer. To determine the Chl-*a* concentrations, the methodological procedures of [31] were followed. Simultaneously with the water sampling, a handheld fluorometer (FluoroProbe, BBE Moldaenke Inc., Schwentinental, Germany) was used. FluoroProbe is a highly sensitive measuring instrument for the analysis of chlorophyll with algae class determination [12,13]: green algae, blue–green algae/cyanobacteria, diatoms/dinoflagellates, and cryptophytes. It uses six excitation lasers, allowing discrimination of algae groups and correcting the results according to the presence of dissolved organic matter and the

turbidity level (of mineral origin) in the waters. To evaluate the agreement between in situ and BBE FluoroProbe Chl-*a* measurements, the Pearson's correlation coefficient was calculated.

2.2. Multispectral Platform: Data Collection and Processing

The multispectral camera used was a Parrot Sequoia (Figure 2b) with 12-megapixel resolution discrete multispectral bands, capturing ~40 nm-wide bands in the green (~550 nm), red (~660 nm), and near-infrared (~790 nm) regions, and one in the red-edge (~735 nm) region with a 10 nm narrowband (Figure 2d). The capture system employs a global shutter. This camera also features a sensor that captures data with a rolling shutter system in RGB with 16-megapixel resolution.

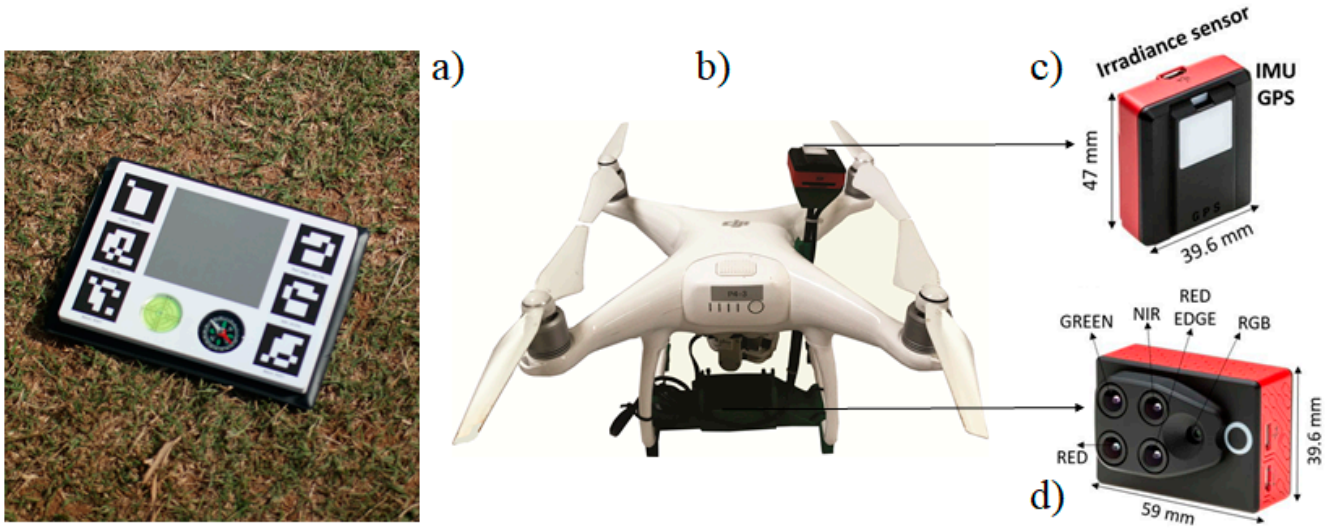

Figure 2. (**a**) Calibration panel, (**b**) Sequoia camera attached to the DJI Phantom 4 using a 3D-printed support, (**c**) irradiance sensor, and (**d**) Sequoia camera and its multispectral and RGB sensors (Parrot Company, Paris, France).

Due to its 135 g weight and small size, Sequoia is versatile and adaptable to various UAV models. Although developed primarily for agricultural applications, it has been tested for water quality monitoring [26,32]. Sequoia features a global positioning system and an inertial measurement unit (GPS/IMU) magnetometer system and an irradiance sensor (Figure 2b). Positioning and camera data, as well as irradiance data, are stored by the camera, facilitating the generation of orthomosaics for multispectral bands with at-sensor surface reflectance (asSR) values.

The Sequoia camera was mounted on the DJI Phantom 4 using a 3D-printed support (Figure 2b). The autonomous flight plan was configured using the Drone Deploy mission planning software at an altitude of 120 m above the ground, with a maximum flight speed of 15 m/s, 80% lateral overlap, and 65% frontal overlap. The entire study area was imaged with 10 flight lines in 11 min, comprising 411 individual images, covering 26 hectares, and consuming only 1 battery. Sequoia provides a communication system via a Wi-Fi network and uses an Internet Protocol code. It can be configured and programmed to acquire images on any device with an internet browser.

The asSR orthomosaics were computationally generated using the digital photogrammetry method, called Structure from Motion (SfM), in Pix4Dmapper software. SfM works with the automatic identification of homologous points on a set of overlapping images through a bundle adjustment procedure [33]. The construction of the orthomosaic in Pix4Dmapper follows these steps: aligning the images, creating the 3D point cloud and the triangular mesh, and the digital elevation model. The asSR values were automatically computed using sensor settings, a sun irradiance sensor, and a calibration panel (Figure 2a).

Sensor settings were retrieved from the Exif metadata for each image, which includes exposure time, shutter speed, vignetting, dark current, and the ISO value. The irradiance sensor (Figure 2c) provides a record of the light conditions during the flight in the same spectral bands as those captured by the multispectral sensor. Images of the calibration panel are required to perform corrections at least once during each flight, as long as sky and illumination conditions remain stable during the acquisitions. Considering overlapping images, Pix4Dmapper calculates the reflectance values for each pixel of the orthomosaics using a weighted average of the pixels in all the original images that correspond to this pixel, but it assigns more weight to images where the pixel is more central (Pix4D S.A.). In this study, the asSR orthomosaics were generated with a ground sampling distance (GSD) equal to 13 cm.

2.3. Hyperspectral Platform: Data Collection and Processing

Headwall Nano-Hyperspec is a hyperspectral sensor weighing 680 g, featuring 276 spectral bands at a 2.2 nm spectral resolution, covering a spectrum range from 400 to 1000 nm. This camera has a 28.1° sensor field of view using a 12-mm lens with a complementary metal-oxide-semiconductor sensor. A subsystem can store 480 GB of the 12-bit radiometric resolution images. The images were acquired by a push-broom scanning system for scanning pixel lines (Headwall Photonics Inc., Bolton, MA, USA). This type of sensor acquires the entire line of the image at once and continuously captures the image with the motion of the drone [24]. The Nano-Hyperspec is integrated with a GPS/IMU system, featuring a GPS antenna and an internal magnetometer that generates the X, Y, and Z coordinate information through the inertial navigation system (Figure 3b).

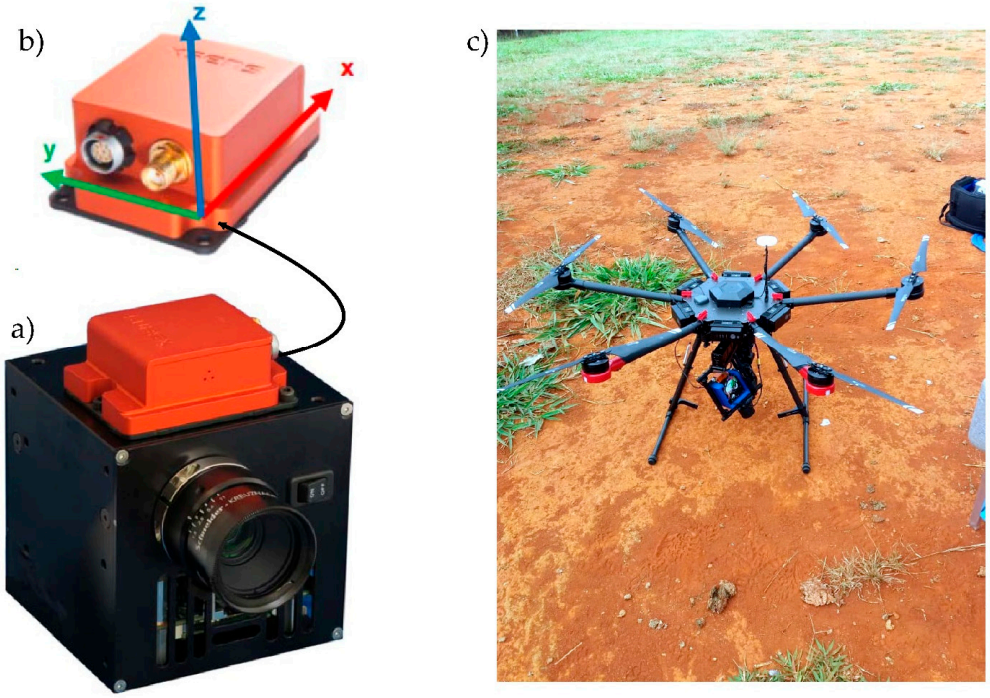

Figure 3. (**a**) Hyperspectral Headwall Nano-Hyperspec (Headwall Photonics Company, Bolton, USA), (**b**) GPS/IMU system, and (**c**) DJI Matrice 600 with Nano-Hyperspec and Gimbal DJI RONIN MX.

Three software applications are integrated into the Nano-Hyperspec camera for configuration and data processing (Headwall Photonics Inc., Bolton, MA, USA). XSENS software ensures effective scanning under sustained vibrations, prolonged accelerations, and magnetic disturbances, and provides trajectory corrections using the GPS/IMU system [34]. Hyperspec III software has several functional configurations: radiometric, geometric, GPS, and automatic trigger settings. Spectral View software has the functions of processing the

acquired images: orthorectification using GPS/IMU system information, conversion of digital numbers to radiance, and spectral visualization of the scanners.

Nano-Hyperspec was installed on a Matrice 600 (M600) hexacopter (DJI Inc., Shenzhen, China). M600 weighs 9.5 kg and can take off with a maximum weight of 15.5 kg (Figure 3c), with a flight autonomy of approximately 25 min. The Nano-Hyperspec camera was coupled to the M600 using a Gimbal (DJI RONIN MX) and a 3D-printed support (Figure 3). Autonomous flights were configured using the DJI Ground Station Pro mission planner software with an altitude of approximately 250 m above the ground, a maximum speed of around 7 m/s with 20% lateral overlap, and 10% frontal overlap to generate orthomosaics with a GSD equal to 17 cm. The flights for both cameras were performed with high solar zenith angle conditions (>45°) to avoid sun glint effects [24,26,35–37].

Digital number images from the Nano-Hyperspec camera were converted to radiance using an internal calibration file that provides gains and offsets for each wavelength band (i.e., radiance = gain × digital number + offset). Spectral View software was used for image orthorectification and image mosaicking. Afterward, the mosaicked radiance images were converted to surface reflectance asSR, computing the ratio between the irradiance and radiance [38], which can be described as follows:

$$\text{asSR} = \frac{L_w(\lambda)}{E_d(\lambda)} \quad (1)$$

where L_w (W m^{-2} nm^{-1} sr^{-1}) is the upwelling radiance, representing the radiance images from the Nano-Hyperspec camera, and E_d (W m^{-2} nm^{-1}) is the downwelling irradiance measured on the ground. E_d was measured simultaneous to the flight acquisitions with a TriOS RAMSES hyperspectral irradiance spectroradiometer pointing at the zenith. This instrument has a spectral resolution of approximately 2 nm, from 320 to 950 nm. Each pixel in the final hyperspectral asSR images was corrected using a filtering method [37] based on a Fourier transformation, to remove high-frequency components [39].

2.4. Chl-a and HABs Algorithms and Analysis of Performances

The entire UAV acquisition methodology was as follows: (a) planning and execution of UAV surveys, (b) field collection of limnological in situ data simultaneous to UAV surveys, (c) image processing to generate asSR orthomosaics, (d) retrieval of the limnological status of each pond, (e) analysis of the statistical performances of bio-optical models against the Chl-*a* and cyanobacteria field data, and (f) Chl-*a* and cyanobacteria mapping using the most robust models for both UAV platforms. The asSR pixel values, a sample of eight pixels, from the multi- and hyper-spectral orthomosaics, were extracted at the same geographic positions of the water sampling points for application of Chl-*a* and cyanobacteria bio-optical models.

The optical properties of water are the basis for the development of bio-optical models for estimating the OAC, such as photosynthetic pigments. Bio-optical models are classified into different categories: empirical, semi-empirical, semi-analytical, quasi-analytical, and analytical [8,40]. There is a wide variety of Chl-*a* and cyanobacteria models applied in inland waters with a large range of concentration levels and with multiple radiometric data sources: spaceborne, airborne, and in situ sensors [4–6].

Chl-*a* was estimated using two-band algorithms that cover wavelengths of maximum (~660–680 nm) and minimum (~700–720 nm) absorption effects, yielding satisfactory results for monitoring this parameter in continental waters. For turbid and productive waters, three-band models between near-infrared (NIR) and red wavelengths have been developed [41]. These models incorporate bands in NIR wavelengths, taking into account the minimal absorption wavelengths of Chl-*a*. In extremely turbid waters, four-band models have been adapted from the three-band models to minimize the absorption and scattering effects of total suspended solids (TSS) [41].

Bio-optical PC models, particularly semi-empirical ones, have also been applied in the literature and share a similar rationale as those for Chl-*a*. Two-band models are employed

as well, but with the aim of identifying the peak and absorption of PC at red wavelengths. Three-band models, on the other hand, are based on the wavelengths that are most and least sensitive to PC absorption, along with a third band that has a negligible influence on this pigment. Spectral indices have also been developed for estimating PC, as well as Chl-*a* [9].

Bio-optical models from the literature were retrieved and adjusted to estimate Chl-*a* and cyanobacteria based on the Headwall Nano-Hyperspec and Parrot Sequoia camera spectral bands. The effectiveness of the models was evaluated using a bootstrap resampling method [42]. Bootstrap and cross-validation are useful statistical tools for validation with small sample sizes. In these methods, the training and testing data of the models are continuously resampled with replacement within the sample distribution. Each data point in the available sample can be resampled multiple times, for both training and testing [43]. Bootstrap resampling was performed 1000 times (number of interactions between training and testing), and the R-squared (R^2), root mean square error (RMSE), and mean absolute error (MAE) mean values of the 1000 interactions were calculated. The equations for R^2, RMSE, and MAE are as follows:

$$\mathrm{RMSE} = \sqrt{\frac{1}{N}\sum_{i=1}^{N}(X - X)^2} \tag{2}$$

$$\mathrm{MAE} = \frac{1}{N}\sum_{i=1}^{N}[X' - X] \tag{3}$$

$$R^2 = 1 - \frac{\sum_{i=1}^{N}[X' - X]^2}{\sum_{i=1}^{N}[X^- - X]^2} \tag{4}$$

where X' represents the UAV-derived values, X^- is the average value of the samples, and X represents the in situ Chl-*a* and cyanobacteria concentrations, with N being the number of data points. Regression results between estimated and in situ-measured parameters were also used to further interpret the retrieval performance of each model: slope, intercept, and R^2.

RMSE was considered a key validation parameter because it represents the average difference between the observed values and the values predicted by the regression model. It provides an estimate of the magnitude of prediction errors and is used to evaluate the performance of the model in absolute terms. The R-squared (R^2) value was calculated to assess the explanatory power of the model in relation to the variation in the observed data. Additionally, the mean absolute error (MAE) was calculated to verify its consistency with the RMSE values.

Geoprocessing tools were utilized to extract the asSR values and to implement the most robust bio-optical model for mapping chlorophyll-a (Chl-*a*) and cyanobacteria within the designated study areas. Figure 4 presents the flowchart illustrating the sequential steps of the methodological procedures employed.

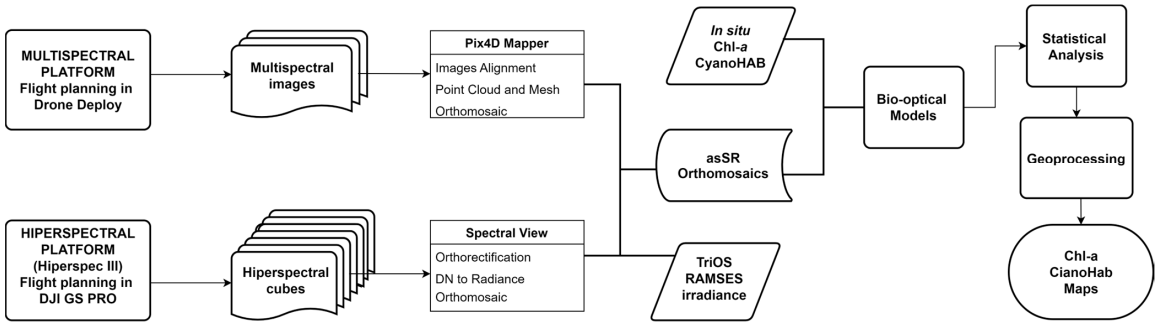

Figure 4. Flowchart of methodological procedures for Chl-*a* and Cyanobacteria mapping andvalidation analysis of the unmanned multispectral and hyperspectral platforms.

3. Results

3.1. Exploratory In Situ Analysis

Table 1 presents the statistics of the limnological data collected by sonde concomitant with the UAV surveys. Overall, higher Chl-*a* concentrations are associated with greater pH, conductivity, temperature, and turbidity values. According to the analyzed data, the BEE fluorometer showed a predominance of green algae, followed by blue–green algae, diatoms, and cryptophyta. FluoroProbe Chl-*a* concentration estimates were compared with water samples processed in the laboratory using the conventional method [40], showing consistency, with a correlation coefficient of 0.9. The highest Chl-*a* concentrations were observed in the ponds corresponding to the sample points 13, 14, and 10 (Figure 1), with concentrations of 244.1, 290.7, and 245.8 µg/L, respectively. Only ponds 1, 7, and 11 showed Chl-*a* levels below the maximum acceptable level for aquaculture in Brazil (i.e., 30 µg/L), considering Class 2, according to Conama Resolution No. 357 of 2005 [44]. The correlation between Chl-*a* and cyanobacteria was 0.55.

Table 1. Summary of the water quality parameters and pigment distribution as registered during the field surveys.

Parameters	Mean *	Median *	Min *	Max *	Std. Deviation *
Chl-*a* (µg/L)	116.31	113.85	14.30	290.70	80.81
Green algae (µg/L)	81.18	84.55	13.98	193.90	48.25
Blue–green algae (µg/L)	22.23	3.10	0.00	112.50	35.36
Diatoms (µg/L)	8.54	5.50	0.09	43.10	10.27
Cryptophyta (µg/L)	4.38	0.01	0.00	20.30	6.63
Yellow substances (µg/L)	0.24	0.00	0.00	3.29	0.75
pH	8.79	9.10	6.30	9.80	0.89
Conductivity (µS/cm)	49.43	51.00	14.40	90.10	18.95
Turbidity (FNU)	40.70	15.90	2.50	366.10	82.56
Temperature (°C)	25.68	25.80	24.00	26.80	0.75

* N = 18.

3.2. Spectral Analysis from Multi- and Hyper-Spectral UAV Platforms

Figure 5 displays the orthomosaic radiance images captured at λ = 832 nm. The calibration process for asSR (apparent surface reflectance) was conducted using Equation (1), resulting in the generation of spatialized reflectance spectral information for 250 bands spanning from λ400 to λ950 nm. It is important to note that although the Nano-Hyperspec camera has 276 bands, the bands with λ > 950 nm were excluded from the calibration process. This decision was made due to the coverage of the Ramses irradiance sensor, which extends up to λ > 950 nm, and the fact that water reflectance becomes null beyond these wavelengths [45]. Figure 6 presents the orthomosaics of the multispectral images obtained using the Sequoia camera in asSR. It is worth noting that flights conducted under both mean and high solar zenith angle conditions resulted in the absence of sun glint in all orthomosaics, as depicted in Figures 5 and 6.

Figure 7 presents the variation of the asSR and the determination coefficient calculated between each spectral value and Chl-*a* and the algae groups (green algae, blue–green algae, diatoms, and cryptophyta). The asSR spectra were extracted over the 18 field sampling points from the calibrated images of the Nano-Hyperspec and Sequoia cameras. Spectral features related to pigment absorption clearly appeared with the ~2 nm spectral resolution of the Nano-Hyperspec camera (Figure 7a), while those patterns were much less clear when considering the four multispectral bands of the Sequoia camera (Figure 7b).

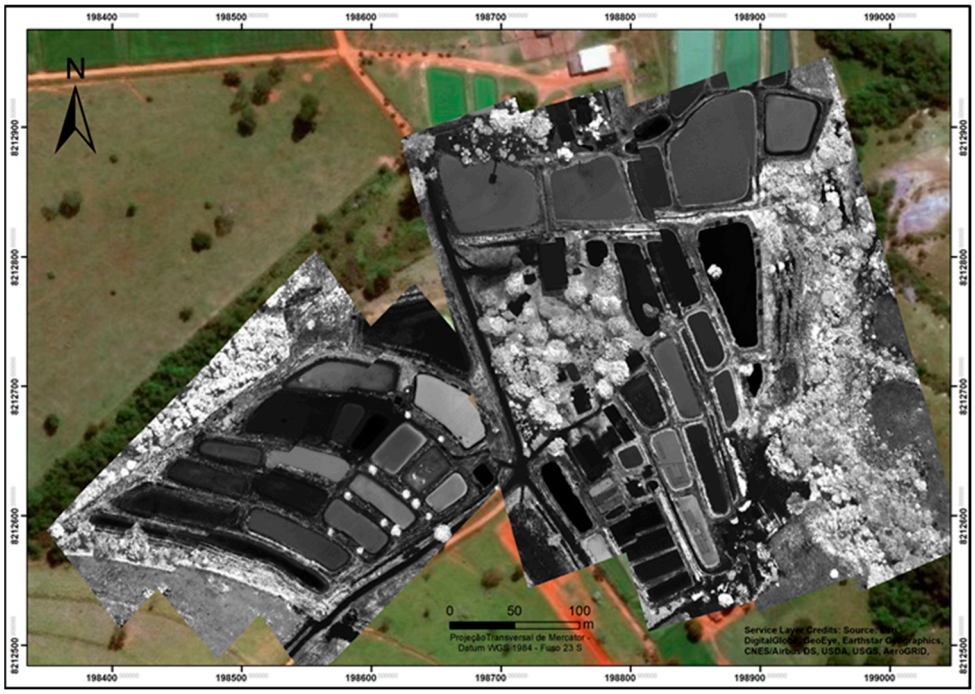

Figure 5. Nano-Hyperspec orthomosaic at λ = 832 nm over the ponds.

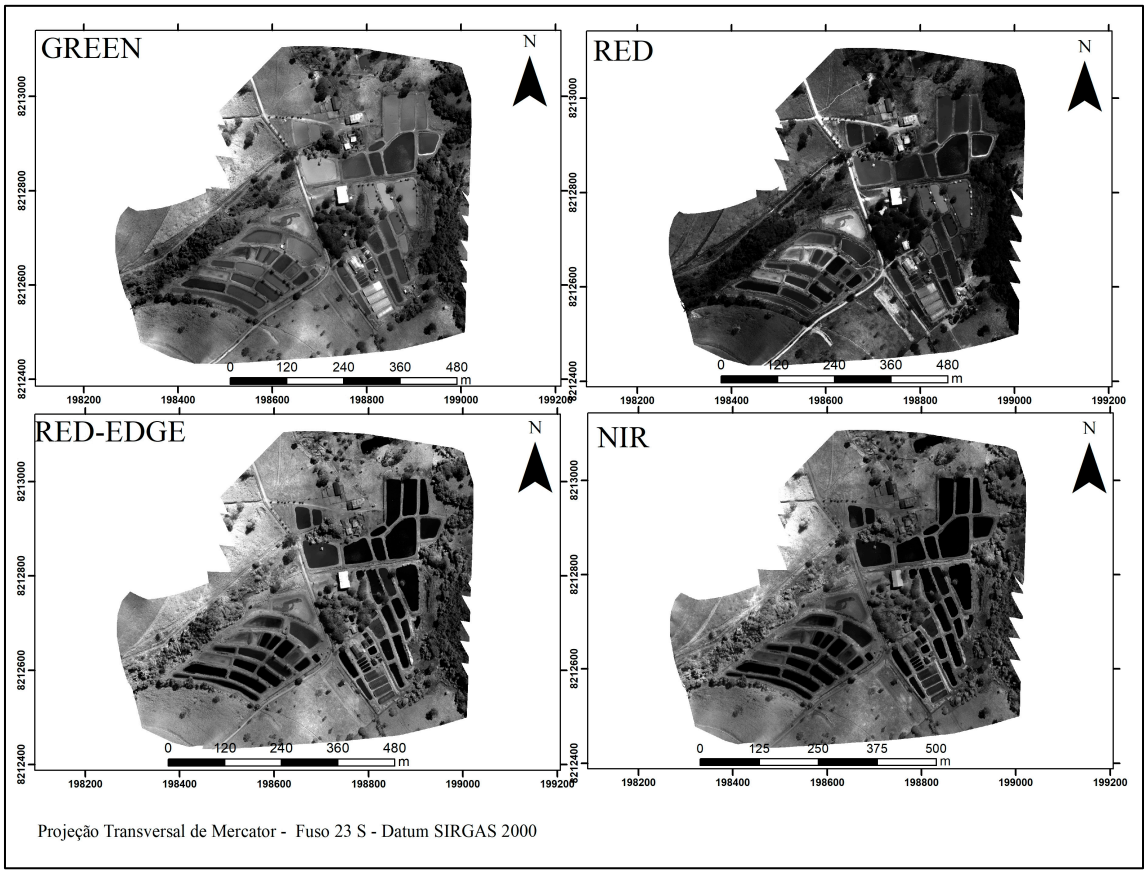

Figure 6. Orthomosaics of the Sequoia bands over the ponds.

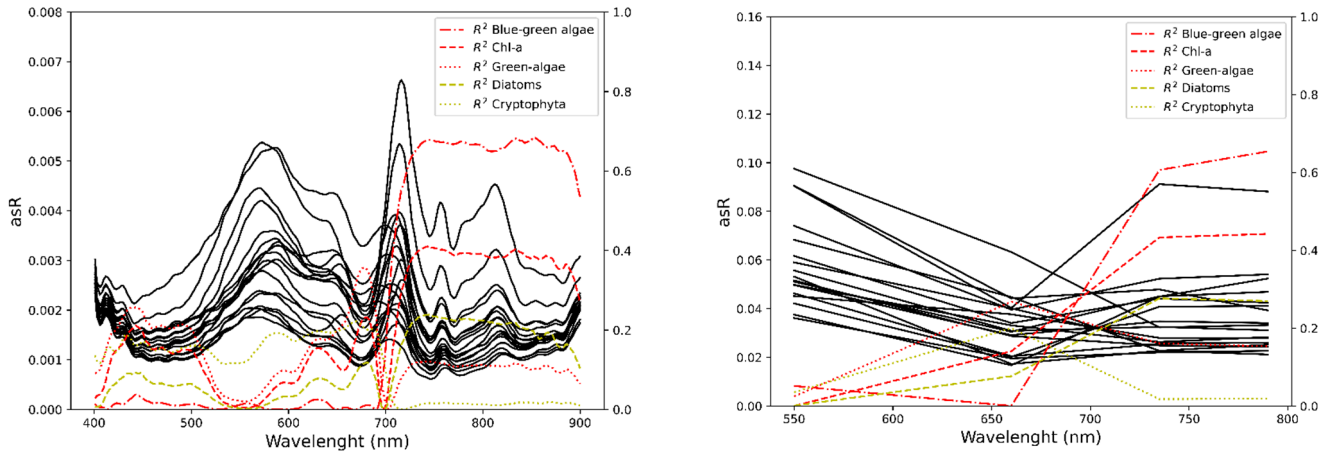

Figure 7. Surface reflectance spectra and R^2 values in relation to the concentrations of the Chl-*a* and the algae groups for each spectral band of the Nano-Hyperspec (**a**) and of the Sequoia (**b**) cameras.

The high spectral resolution of Nano-Hyperspec (Figure 7a) allowed extracting the water's spectral signatures with limited noise after the application of the Fourier filter. Numerous previous works related the reflectance trough at 440 nm with the Chl-*a* absorption maximum in the same spectral range. Correspondingly, the reflectance maximum between λ550 and λ555 nm was probably induced by the Chl-*a* absorption minimum in the same spectral range. At larger wavelengths, the maximum Chl-*a* absorption feature in the red region (λ660 to λ680 nm) induced a reflectance local minimum, which was followed by an absorption minimum within λ700–λ730 nm, reported extensively in the literature to be linked to Chl-*a* optical properties [46,47]. Regarding phycocyanin, in some spectral features, it was possible to observe an absorption feature near λ620 nm and a peak scattering near λ650 nm, as reported in the literature for aquatic environments containing cyanobacteria [24,48,49].

Figure 5b displays the asSR spectra acquired using Sequoia's multispectral camera. Due to the camera's low spectral resolution, the optical features induced by the phytoplankton pigments were hardly visible. However, the reflectance behavior from the green (~λ550 nm) to the NIR (~λ790 nm) spectra well-matched the reflectance variation recorded using the hyperspectral camera, resulting in a determination coefficient value between SR^{-1} and Chl-*a* concentrations almost similar for both cameras.

3.3. Chl-a Bio-Optical Models from Multi- and Hyper-Spectral UAV Platforms

Twenty-seven Chl-*a* bio-optical models were tested (Table 2). The high spectral resolution of the Nano-Hyperspec camera made it possible to test a broad variety of models, including models developed from in situ hyperspectral spectroradiometer data. The lower spectral resolution of the Sequoia camera did not enable testing such a diversity of models (Table 2). For most models applied, some adaptations were made to fit the spectral ranges of the Sequoia bands.

Among the various types of models considered for Chl-*a* and CyanoHAB mapping, including two-band, three-band, indexes, and semi-analytical models, at least one model from each group exhibited high performance across different statistical categories; notably, model #1 (RMSE: 32.8 µg/L), model #2 (RMSE: 33.1 µg/L), and model #7 (RMSE: 32.9). Based on the information provided, it is stated that model #1 was chosen for Chl-*a* mapping due to its low RMSE value (considered a decisive parameter) and high R^2 value. A lower RMSE value indicates better accuracy in predicting Chl-*a* concentrations, while a higher R^2 value suggests a stronger correlation between the model's predictions and the actual Chl-*a* values. These best-performing models (#1, #2, and #7) could not be utilized for the

Sequoia camera due to limitations in its spectral resolution. In Table 2, it is demonstrated that the adapted Normalized Difference Chlorophyll Index (NDCI) model #14 emerged as the most effective model for the multispectral configuration, (RMSE: 47.6 µg/L). Therefore, the adapted NDCI model (#14) was selected as the most suitable option for Chl-*a* mapping using the Sequoia camera. Additional statistical details regarding the bio-optical Chl-*a* models throughout the bootstrap process are presented in Table A1 of Appendix A.

Table 2. Chl-*a* bio-optical models and their statistical results.

Code	Model Algorithm	Nano-Hyperspec			Parrot Sequoia			Ref.
		R^2	RMSE	MAE	R^2	RMSE	MAE	
	Two-band NIR and Red models							
1	**SR_{716}/SR_{676}**	**0.87**	**32.8**	**25.7**		Not applicable		
2	SR_{709}/SR_{665}	0.86	33.1	26.8		Not applicable		[24]
3	SR_{705}/SR_{665}	0.84	36.8	29.8		Not applicable		[50]
4	SR_{740}/SR_{665} *	0.81	38.7	29.8	0.59	57.7	42.0	[51]
5	$SR_{666}{}^{-1} \times SR_{704}$	0.81	39.7	32		Not applicable		[52]
6	$SR_{665}{}^{-1} \times SR_{783}$ *	0.78	39.7	32.8	0.28	72.5	52.4	[41]
	Three-band NIR and Red models							
7	$(SR_{666}{}^{-1} - SR_{704}{}^{-1}) \times SR_{723}$	0.86	32.9	25.6		Not applicable		[52]
8	$(SR_{665}{}^{-1} - SR_{705}{}^{-1}) \times SR_{740}$	0.84	35.0	27.0		Not applicable		[53]
9	$(SR_{665}{}^{-1} - SR_{705}{}^{-1}) \times SR_{783}$ *	0.83	36.9	28.2	0.44	65.5	46.6	[51]
10	$(1/SR_{670} - 1/SR_{710}) \times SR_{750}$	0.83	36.1	28.0		Not applicable		[54]
11	$(SR_{665}{}^{-1} - SR_{708}{}^{-1}) \times SR_{753}$	0.84	36.2	28.1		Not applicable		[55]
12	$(1/SR_{660} - 1/SR_{708}) \times SR_{755}$	0.83	37.3	29.0		Not applicable		[23]
	Index models							
13	FLH: $SR_{680} - [SR_{665} + (SR_{708}/SR_{665}) \times ((\lambda_{680} - \lambda_{665})/(\lambda_{708} - \lambda_{665}))]$	0.86	35.2	28.5		Not applicable		[56]
14	**NDCI: $(SR_{708} - SR_{665})/(SR_{708} + SR_{665})$ ***	0.82	38.6	31.4	**0.72**	**47.6**	**37.0**	[57]
15	BNDVI: $(N - B)/(N + B)$	0.67	52.2	42.1		Not applicable		[58]
16	INDEX: $(SR_{665}{}^{-1} - SR_{708}{}^{-1})/(SR_{753}{}^{-1} + SR_{708}{}^{-1})$	0.67	53.2	39.7		Not applicable		[59]
17	SABI: $(N - R)/(B + G)$	0.6	56.8	46.5		Not applicable		[60]
18	NDVI: $(N - R)/(N + R)$	0.56	59.9	49.3	0.66	52.1	41.0	[61]
19	AI: $((SR_{850} - SR_{660})/(SR_{850} + SR_{660})) + ((SR_{850} - SR_{625})/(SR_{850} + SR_{625}))$	0.56	61.3	51.6		Not applicable		[62]
20	GNDVI: $(N - G)/(N + G)$	0.36	73.8	61.6	0.40	68.1	56.7	[17]
21	NGRDI: $(G - R)/(G + R)$	0.29	74.8	61.6	0.37	73.1	57.9	[63]
22	KIVU: $(B - R)/G$	0.20	82.9	68.0		Not applicable		[64]
23	GLI: $(2 \times G - R - B)/(2 \times G + R + B)$	0.14	82.8	70.3		Not applicable		[65]
24	NGBDI: $(G - B)/(G + B)$	−0.05	89.3	74.8		Not applicable		[66]
25	EXG: $2 \times G - R - B$	0	91.7	76.9		Not applicable		[67]
	Semi-analytical models							
26	$[35.7 \times (SR_{708}/SR_{665}) - 19.3]^{1.124}$ *	0.86	34.3	27.6		Not applicable		[65]
27	$(SR_{662} - SR_{693})/(SR_{740} + SR_{705})$ *	0.14	89.4	72.3		Not applicable		[66]

* Adapted for Sequoia bands.

Chl-*a* maps were generated from the best retrieval model for the multi- and hyperspectral images (Figure 8). Most ponds showed elevated Chl-*a* concentrations, and the maps produced from both airborne systems showed consistent results. In several ponds, the Chl-*a* levels were above the maximum acceptable concentration for aquaculture in Brazil, that is 30 µg/L, for Class 2, according to Conama Resolution No. 357 of 2005 [44].

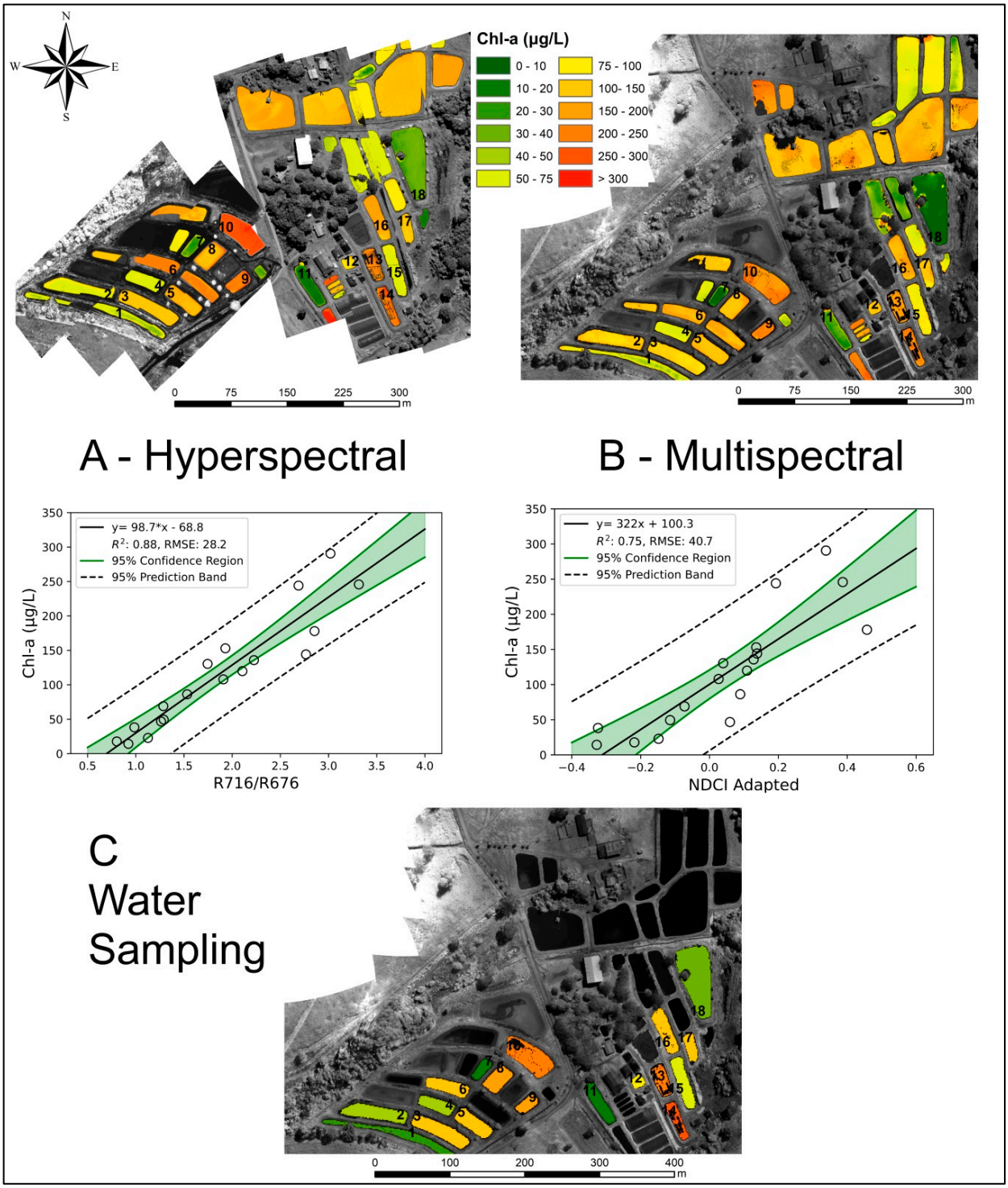

Figure 8. Chl-*a* maps in the fish-farming ponds generated by the Nano-Hyperspec (**A**), Sequoia (**B**), and in situ data (**C**).

3.4. Cyanobacteria Bio-Optical Models from Multi- and Hyper-Spectral UAV Platforms

Cyanobacteria (blue–green algae) bio-optical models are not as widely disseminated in the literature as those designed for Chl-*a* retrieval. However, cyanobacteria retrieval models are receiving growing attention, mainly because they make it possible to detect HABs [24,67–69]. Table 3 presents 14 retrieval models that were analyzed in this work using hyperspectral data.

According to the provided information, the cyanobacteria models generated using the Nano-Hyperspec camera showed favorable statistical results, as indicated in Table 3. Among the considered models, model #35 exhibited the best performance, characterized by a low RMSE value and a high R^2 value. Consequently, model #35 was selected for mapping cyanobacteria levels in the ponds, and this mapping is illustrated in Figure 9A.

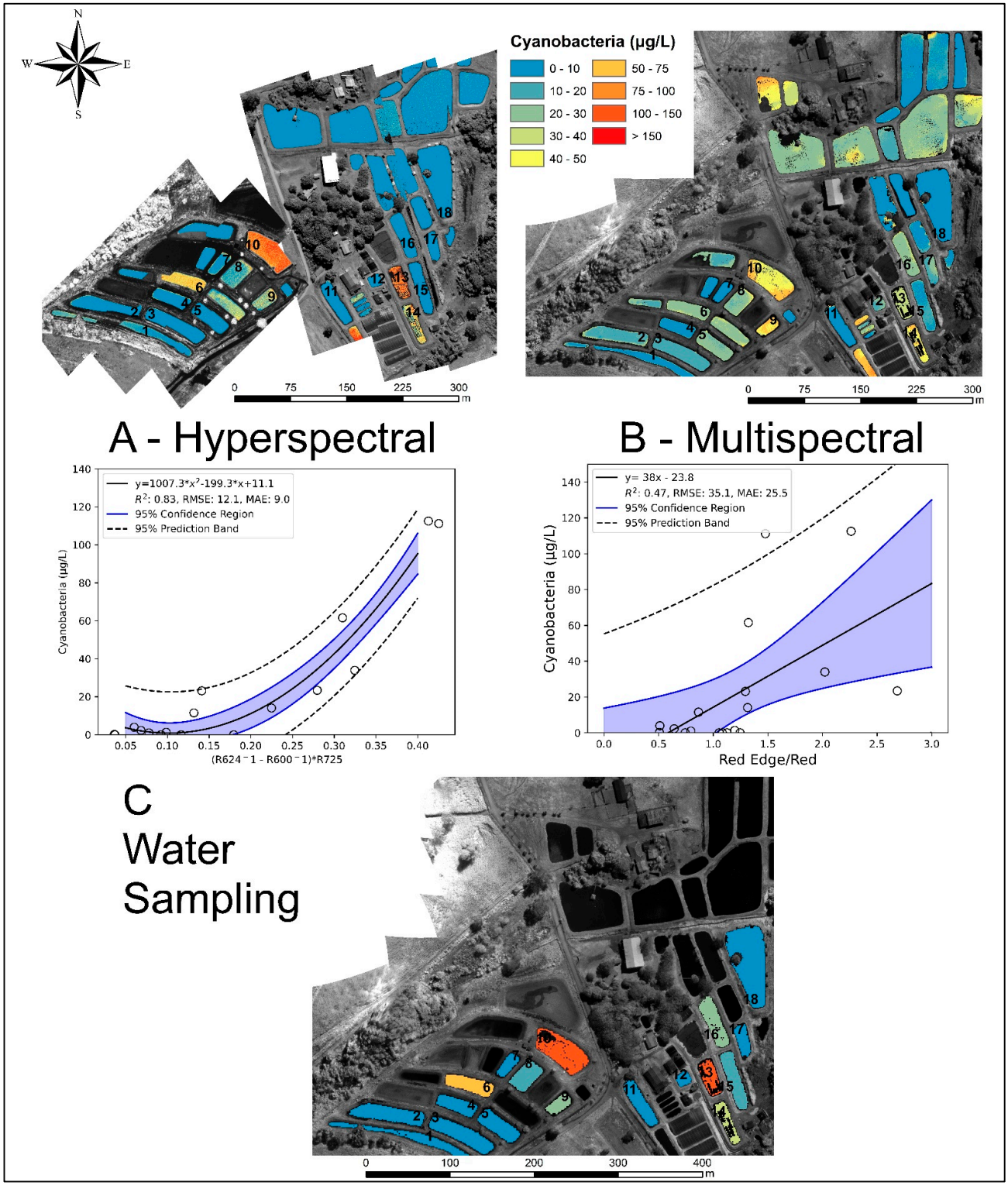

Figure 9. Cyanobacteria maps in the fish-farming ponds generated by the Nano-Hyperspec (**A**), Sequoia (**B**), and in situ data (**C**).

It is stated that cyanobacteria models require a higher spectral resolution compared to Chl-*a* models. Consequently, only two models were suitable for the Sequoia camera (Table 2). However, these two models adapted for the Sequoia camera failed to achieve acceptable statistical performances, with an R^2 value below 0.5 and an RMSE value higher than 35 µg/L. In contrast, the bio-optical model (model #34) applied to the Sequoia camera (Figure 9B) resulted in an RMSE approximately 200% higher than that of the model used with the hyperspectral camera (model #35). These results show that the hyperspectral camera outperformed the multispectral camera in monitoring cyanobacteria, offering a higher accuracy. Therefore, it can be inferred that the hyperspectral camera is better suited for accurately monitoring cyanobacteria compared to the Sequoia camera. For additional statistical details of the bio-optical Chl-*a* model and the bio-optical cyanobacteria models during the bootstrap process, please refer to Tables A1 and A2, respectively, in Appendix A.

Table 3. Cyanobacteria bio-optical models and their statistical results.

Code	Model Algorithm	Nano-Hyperspec			Parrot Sequoia			Ref.
		R^2	RMSE	MAE	R^2	RMSE	MAE	
	Two-Band Models							
28	SR_{708}/SR_{622}	0.73	13.5	9.5		Not applicable		[23]
29	SR_{710}/SR_{620}	0.64	14.0	10.2		Not applicable		[24]
30	SR_{709}/SR_{600}	0.55	15.1	10.8		Not applicable		[68]
31	SR_{700}/SR_{600}	0.71	20.0	13.5		Not applicable		[70]
32	SR_{724}/SR_{600}	0.04	21.0	14.2		Not applicable		[15]
33	SR_{650}/SR_{625}	0.61	28.9	21.9		Not applicable		[71]
34	SR_{724}/SR_{660} *	0.39	34.6	24.5	**0.47**	**35.1**	**25.5**	[72]
	Three-band NIR and Red models							
35	$\mathbf{(SR_{624}{}^{-1} - SR_{600}{}^{-1}) \times SR_{725}}$	**0.83**	**12.1**	**9.0**		Not applicable		[73]
36	$(1/SR_{622} - 1/SR_{708}) \times SR_{755}$ *	0.56	15.6	10.8	0.27	37.2	26.7	[23]
37	$(SR_{615}{}^{-1} - SR_{600}{}^{-1}) \times SR_{725}$	0.65	15.5	11.5		Not applicable		[74]
	Index models							
38	PCI: $SR_{555} - (SR_{555} - SR_{665})/(\lambda_{655} - \lambda_{555}) \times (\lambda_{630} - \lambda_{555}) - SR_{630}$	0.52	19.8	14.1		Not applicable		[75]
39	SLH: $SR_{714} - [SR_{654} + ((SR_{754} - SR_{654})/(\lambda_{754} - \lambda_{654})) \times (\lambda_{714} - \lambda_{654})]$	0.68	33.4	22.8		Not applicable		[76]
40	CI: $SR_{681} - SR_{665} - (SR_{709} - SR_{665}) \times ((\lambda_{681} - \lambda_{665}))/(\lambda_{709} - \lambda_{665}))$	0.64	32.5	22.7		Not applicable		[76]
41	$(SR_{556} - SR_{510})/(\lambda_{556} - \lambda_{510})$	0.51	38.8	27.8		Not applicable		[77]

* Adapted for Sequoia bands.

4. Discussion

4.1. Retrieval of Water Quality in the Artificial Ponds

The Chl-*a* levels in the ponds were mostly above what the Brazilian environmental resolution endorses, indicating the need for remediation. Concerning the Chl-*a* concentration, fifteen out of eighteen ponds had concentrations above 30 µg/L based on the field water samplings. Both hyperspectral and multispectral cameras successfully detected those fifteen ponds, but the Sequoia camera produced one false-positive detection. Examining the most eutrophic ponds, the hyperspectral camera and water samplings revealed that ten out of eighteen ponds had a Chl-*a* concentration above 100 µg/L. The multispectral camera successfully detected those ten ponds as well, but it erroneously attributed two additional ponds to the upper range of concentrations. Finally, while water samplings revealed that only ponds 1, 7, and 11 (Figure 1) had Chl-*a* concentrations below 30 µg/L, the hyperspectral camera retrieved Chl-*a* concentrations below 30 µg/L for ponds 7, 11, and 18. For the lower range of Chl-*a* concentrations, the Sequoia camera detected only two ponds (7 and 18). We assessed that fourteen out of eighteen ponds were correctly mapped

regarding their eutrophic status using the hyperspectral camera when compared to field monitoring. The same fourteen ponds were also correctly mapped with the multispectral camera, demonstrating that the Sequoia camera enabled satisfying monitoring results. The primary differences between both airborne sensors were the slightly larger number of false-positive detections of some eutrophic ponds and the lower accuracy in detecting oligotrophic conditions.

Regarding cyanobacteria, field water measurements detected four ponds with concentrations above 30 µg/L, of which two ponds had concentrations above 100 µg/L (i.e., ponds 10 and 13). The hyperspectral camera mapped 5 out of the 18 surveyed ponds with concentrations above 30 µg/L, of which 2 ponds were mapped with concentrations above 100 µg/L (i.e., ponds 10 and 13). The multispectral camera successfully classified only three ponds with cyanobacteria concentrations above 30 µg/L but failed to detect the two most eutrophic ponds (i.e., above 100 µg/L).

4.2. Chl-a Retrieved from Multi- and Hyper-Spectral UAV Platforms

Table 2 demonstrates the unquestionable capacity of the Nano-Hyperspec camera to support the use of a wide variety of Chl-*a* bio-optical models. Of the twenty-seven models tested, fourteen obtained $R^2 > 0.8$. It is worth noting that almost all of the fifteen most robust models utilized narrow bands between 660 and 730 nm, highlighting the importance of an ideal sensor having at least two bands covering both the absorption peaks at ~660–680 nm and the reflectance maximum at ~700–730 nm from Chl-*a* [78]. Several studies have tested and confirmed the efficiency of bio-optical models using spectral bands at those wavelengths to estimate Chl-*a* in continental waters [12,13,41,79–84]. It is worth mentioning that the authors of [13] concluded that there is no universal model for estimating Chl-*a*, as most models perform better for specific concentration ranges and/or water types and/or for a given location, but not for another set of conditions. Our results showed that the hyperspectral camera has high potential for Chl-*a* monitoring using drone platforms, as it allows the use of a large variety of retrieval models that may be selected according to the pond-specific conditions.

The Sequoia camera does not offer multiple spectral bands at red and NIR wavelengths, but its spectral resolution may be adequate to capture spectral patterns related to the presence of photosynthetic pigments, allowing for reliable estimates for Chl-*a*. The Sequoia red band extends from 640 to 680 nm and is partly impacted by the Chl-*a* light absorption maximum from 660 to 680 nm. The red-edge band covers a narrow wavelength range from 730 to 740 nm that is partly impacted by the Chl-*a* reflectance peak. We examined the bio-optical models that could be used for both hyperspectral and multispectral cameras, such as models #4, #6, #9, and #14 (Table 2). Those models were modified for the multispectral camera to match the spectral bands but retained their mathematical expression. We observed that the multispectral models presented an average RMSE value that was 56.1% higher than when using their hyperspectral forms. In particular, multispectral forms of models #4, #6, #9, and #14 reached RMSE values 48.4%, 73.4%, 78.8%, and 24% higher in comparison to their hyperspectral forms, respectively. From a user perspective, this difference in Chl-*a* retrieval performance may be evaluated as significant but should be assessed more generally, also considering drone deployment flexibility and investment costs (see Section 4.4).

The best statistical adjustment of the tested models for the Sequoia camera was model #14, which is an adaptation of the NDCI model followed by the NDVI model. NDCI is an index created to determine Chl-*a* over turbid and productive waters that uses a mathematical expression similar to the NDVI index previously developed for terrestrial vegetation. It was originally developed for medium-spectral resolution imaging spectrometer (MERIS) images using 708 nm and 665 nm bands [57]. For our study, the NDCI model adapted to the Sequoia camera used the red-edge and red bands, generating the best statistical performance for the Sequoia camera, and was used to estimate Chl-*a* in the fishponds (Figure 8).

The results demonstrated advances in UAV platforms for accurate Chl-*a* monitoring. Considering the strong eutrophic conditions in the monitored ponds (i.e., mean in situ Chl-*a* concentration of 116.31 µg/L), the best retrieval performances for the Nano-Hyperspec camera (model #1) were considered consistent with other remote sensing-based mapping methods. Although less accurate, the results for the Sequoia camera (model #14) were also consistent, considering studies in the literature using satellite images. The authors of [81] reported a MAPE of 41.2% using Sentinel 2 MSI and a MAPE of 57.3% using Landsat 8 OLI. The authors of [85] reported an R^2 of 0.49 and an RMSE of 48.5% using Sentinel 2 images. Field spectroradiometers may allow for achieving a better performance, such as the results presented in [83], with a MAPE of 16.6%, by the authors of [86], who obtained an R^2 of 0.78 and an RMSE of 10.4 µg/L, and by the authors of [87], who found an R^2 from 0.82 to 0.85 and an RMSE from 45.3% to 52.5%, simulating Sentinel-2 bands. However, the use of field spectroradiometers is much more limited in terms of surface coverage when compared to UAV platforms.

A low Chl-*a* concentration (i.e., below 10 µg/L) may result in degraded retrieval performances, as the spectral patterns are much more subtle, leading to a lower signal-to-noise ratio. However, fine Chl-*a* retrieval over oligotrophic conditions is considered much less critical than the detection of eutrophic conditions concerning licensing requirements by environmental stakeholders. The Brazilian National Council of the Environment's (CONAMA) 30 µg/L threshold for fish-farming activities in freshwaters confirms the importance of focusing on the detection of this Chl-*a* concentration range as a critical operational issue.

4.3. Cyanobacteria Retrieved from Multi- and Hyper-Spectral UAV Platforms

Unlike Chl-*a* retrieval, a fine spectral resolution is considered essential for cyanobacteria and HAB mapping, as all bio-optical models available in the literature require narrow spectral bands within the 600–625 nm spectral domain. In most cases, multispectral cameras do not offer specific bands at these wavelengths, such as the Sequoia camera, which was primarily developed for agricultural applications.

The results in Table 3 confirmed that an ideal multispectral camera for cyanobacteria monitoring must offer a narrow band located in the 600–625 nm range, in addition to another spectral band in the red-edge spectrum, to provide accurate assessments. Of all fourteen models tested with the hyperspectral camera for cyanobacteria retrieval (Table 3), only two models could be adapted to the Sequoia multispectral camera's spectral configuration. Model #34 was adapted from the original SR_{724}/SR_{660} two-band model for the multispectral configuration. Model #34 performed poorly for both hyperspectral and multispectral cameras, with RMSE values around 35 µg/L. Model #36, based on a three-band model, was also adapted to the multispectral configuration. This model exhibited a higher performance with the Nano-Hyperspec camera (R^2: 0.56) than with the Sequoia camera (R^2: 0.27). Despite the low statistical performance, model #34 was used to map cyanobacteria with the Sequoia camera, using the red-edge/red band ratio. Additional research should be carried out with refined sensors for precise detection using multispectral cameras.

As with Chl-*a*, the results in Table 3 also demonstrate the high potential of the Nano-Hyperspec camera to apply several cyanobacteria/HAB bio-optical models. Of the 14 models tested, 3 models obtained an $R^2 \geq 0.7$, with emphasis on models #35, #28, and #29 (various studies have also tested and validated the efficiency of these models for estimating cyanobacteria/HAB in continental waters [9,88–91]. The three-band model (model #35) originally proposed in [73] was robustly applied for monitoring cyanobacteria in fish-farming tanks, showing results compatible with those presented in this study.

4.4. Benefits and Costs of Multi- and Hyper-Spectral UAV Platforms

The robust models used with the hyperspectral camera for Chl-*a* and cyanobacteria monitoring achieved a correlation with in situ samplings of 0.87 and 0.83, respectively, under a bootstrap method of 1000 interactions. For the multispectral camera, the robust

models achieved a correlation of 0.72 for Chl-*a* and 0.47 for cyanobacteria. Undoubtedly, hyperspectral platforms are ideal for the robust monitoring of Chl-*a* and HABs since they provide the applicability of a wide range of models that demand a high spectral resolution. Similar results were also obtained in [24] for cyanobacteria by phycocyanin detection using hyperspectral imagery. Multispectral systems may be regarded as an interesting alternative perspective for Chl-*a* detection, as they are flexible and low-cost platforms, making it possible to map at a very high resolution (~13 cm spatial resolution in this work), ideal for small artificial ponds. It is worth noting that the hyperspectral platform used in this work has a cost ten times higher than the multispectral platform (Table 4).

Table 4. Cost comparison between the multi- and hyper-spectral UAV platforms used in this study.

Devices	Weight (kg)	Cost in USD (×1000)	Devices	Weight (kg)	Cost in USD (×1000)
Parrot Sequoia with irradiance sensor	0.25	4	Headwall Nano-Hyperspec Package	0.68	80
DJI Phantom 4 UAV	0.9	2			
UAV Battery	0.47	0.1	DJI Matrice 600 UAV	5.9	4
Blank row					
Pix4Dmapper Software		2	Battery package	4.1	1
3D support	0.1	0.2			
			DJI GIMBAL RONIM MX	2.2	1.5
			3D support	0.1	0.1
Total	1.7	8.6	Total	~13	86.6

The current cost of hyperspectral platforms can be a strong limiting factor, limited to the financial viability of users' projects. Consequently, the use of multispectral platforms is a sustainable alternative for inland waters, in particular if the sensor used covers the wavelengths related to the light maximum and minimum peak absorption of Chl-*a* and cyanobacteria pigments in the 600–750 nm spectral range.

In addition to methodological and financial issues, it is still necessary to consider operational and technical issues. In general, hyperspectral cameras have a much greater weight (Table 4) and thus demand more robust UAVs than multispectral cameras. Moreover, hyperspectral push-broom cameras, such as the Nano-Hyperspec, have a more complex scanner imaging system. To generate a good-quality image, the UAV must fly at a constant speed and height, harmonized with the trigger configuration of the camera during the scanning process. Considering multispectral cameras' low-weight characteristics, such as the Sequoia camera, these models are versatile and adaptable to light, low-cost, and easy-to-handle UAVs. Thus, considering the practical aspects regarding the operational issues, multispectral platforms appear, once again, as a rational pick for monitoring phytoplankton in inland waters.

We analyzed how UAV platforms compare to other methods that may be used for Chl-*a* and cyanobacteria monitoring, including conventional methods. Considering satellite data, no space-borne platforms are currently simultaneously delivering low costs and high spatial, temporal, and spectral resolutions. Our results confirmed that UAVs can achieve enhanced retrieval performances in comparison to spaceborne platforms. Additionally, the satellite data quality may be hampered by complex atmospheric conditions, requiring precise corrections. Another advantage of UAVs is related to the limitation of satellite data during cloudy days, which may dramatically reduce the availability of orbital images during the rainy season in tropical areas [10,26,45].

Lastly, field spectroradiometer systems allow for obtaining precise spectral curves over individual points and applying a large range of bio-optical models. However, pointwise surveys are limited in characterizing the spatial heterogeneity of water bodies compared to UAVs.

5. Conclusions

The recent and continuous developments of UAVs and small cameras with different spectral resolutions and imaging systems promote new remote sensing platforms that enable water quality monitoring at high spatial and temporal resolutions. These platforms are especially well-suited for small areas where it is difficult to rely on manned airborne or orbital platforms, such as aquaculture ponds.

UAV remote sensing platforms, combined with the application of bio-optical models, provide a robust and practical tool for monitoring the spatial distribution of Chl-*a* and cyanobacteria concentrations in inland water bodies. However, spectral resolution is critical for high-accuracy assessments. The Nano-Hyperspec camera can estimate Chl-*a* and cyanobacteria concentrations more accurately than the Sequoia camera (the hyperspectral camera improved the RMSE value by 14.8 µg/L and 21.6 µg/L for Chl-*a* and cyanobacteria, respectively, in relation to the multispectral camera). Nevertheless, this work demonstrated that a low-cost configuration allows for denser monitoring over areas that are difficult to survey due to the limited spatial resolution of satellite images. This supports the definition of a practical and robust automatic monitoring system for water quality in fish-farming ponds.

Nano-Hyperspec is an excellent camera for monitoring Chl-*a* and cyanobacteria with high precision. However, its integrated platform has a high cost (i.e., ten times greater than the Sequoia platform) that may be inaccessible to projects or users with limited resources. Thus, more accessible multispectral platforms, such as the Parrot Sequoia camera, can be used for monitoring these parameters with moderate precision. For a more precise assessment with multispectral platforms, we recommend using a multispectral camera with specific narrow bands between 660–690 nm and 700–730 nm for Chl-*a*, and between 600–625 nm and 700–725 nm for cyanobacteria. Our results suggested that including UAV imagery as part of the conventional monitoring practices for fish farming has significant potential that deserves further exploration.

Author Contributions: D.O., conceptualized the work (methodology, data acquisition, analysis, and validation) and wrote the original draft of the manuscript; R.C. (Rejane Cicerelli), conceptualized the work (methodology, analysis, and validation) and helped to write the original draft of the manuscript; H.R., participated in the project administration, funding acquisition, supervision, and writing—review; J.-M.M., participated in the planning of the work and the manuscript, data analysis, validation, data curation, and writing—review and editing; T.A., participated in supervision and writing—review; H.B., participated in the field data acquisition, data analysis, and visualization; R.C. (Raphael Casari), participated in the construction of the airborne multispectral platform and flight execution. All authors have read and agreed to the published version of the manuscript.

Funding: This research was funded by Financiadora de Estudos e Projetos (FINEP), grant number: 01.14.0114.00; by the Fundação de Amparo a Pesquisa do Distrito Federal (FAPDF), grant numbers: 23547.93.27555.30052018, 17457.78.36995.26042017, and 00193.00001143/2021-15; and by the Coordenação de Aperfeiçoamento de Pessoal de Nível Superior, Brasil (CAPES), Finance Code 001.

Acknowledgments: We acknowledge the partner institutions that integrate the AQUASENSE research group (http://aquasense.igd.unb.br/ accessed on 12 June 2023). The AQUASENSE group is formed by management and research institutions from Brazil and France that contemplate a water quality monitoring network using multiscale remote sensing techniques.

Conflicts of Interest: The authors declare no conflict of interest.

Appendix A

Table A1. More detailed statistical results of the Chl-*a* bio-optical models.

Code	Model Algorithm	Nano-Hyperspec				Parrot Sequoia *				Ref.
		Est.	Std. e.	Min.	Max.	Est.	Std. e.	Min.	Max.	
	Two-band NIR and Red models									
1	**SR_{716}/SR_{676}**						Not applicable			
	Intercept	−68.9	15.2	−110.1	−32.3					
	coefficient	98.8	11.1	72.5	128.1					
2	SR_{709}/SR_{665}						Not applicable			[20]
	Intercept	−124.9	21.2	−183.5	−68.1					
	coefficient	147.6	15.7	106.7	187.7					
3	SR_{705}/SR_{665}						Not applicable			[46]
	Intercept	−175.6	29.5	−252.4	−99.2					
	coefficient	189.1	22.0	129.1	244.6					
4	SR_{740}/SR_{665}									[47]
	Intercept	−41.6	19.2	−86.4	−12.5	−35.3	35.9	−131.8	37.4	
	coefficient	195.4	28.7	126.9	262.6	125	34.5	68.4	221.5	
5	$SR_{666}^{-1} \times SR_{704}$						Not applicable			[48]
	Intercept	−212.4	38.9	−325.6	−123					
	coefficient	221.3	29.4	149.2	302.6					
6	$SR_{665}^{-1} \times SR_{783}$									[38]
	Intercept	−43.4	21.7	−98.6	8.7	−18.1	45.4	−122.0	64.6	
	coefficient	191.8	30.6	122.2	267.1	110.8	42.5	47.4	207.9	
	Three-band NIR and Red models									
7	$(SR_{666}^{-1} - SR_{704}^{-1}) \times SR_{723}$						Not applicable			[38]
	Intercept	25.3	7.1	8.4	44.8					
	coefficient	174.3	19.8	123.9	224.2					
8	$(SR_{665}^{-1} - SR_{705}^{-1}) \times SR_{740}$						Not applicable			[49]
	Intercept	29.6	8.0	11.6	51.4					
	coefficient	281.2	36.7	195.7	368.9					
9	$(SR_{665}^{-1} - SR_{705}^{-1}) \times SR_{783}$									[47]
	Intercept	29.3	8.5	9.11	53.2	91.7	9.1	69.8	123.5	
	coefficient	274.8	37.2	189.7	366.2	115.6	39.6	54.7	215.9	
10	$(1/SR_{670} - 1/SR_{710}) \times SR_{750}$						Not applicable			[50]
	Intercept	29.9	7.4	11.6	55.8					
	coefficient	210.1	26.3	142.4	281.1					
11	$(SR_{665}^{-1} - SR_{708}^{-1}) \times SR_{753}$						Not applicable			[51]
	Intercept	31.2	8.6	12.1	55.5					
	coefficient	257.2	35.3	178.4	338.1					
12	$(1/SR_{660}^{-1}/SR_{708}) \times SR_{755}$						Not applicable			[52]
	Intercept	38.1	7.6	20.9	59.7					
	coefficient	281.3	37.7	190.9	369.2					
	Index models									
13	FLH: $SR_{680} - [SR_{665} + (SR_{708}/SR_{665}) \times ((\lambda_{680} - \lambda_{665})/(\lambda_{708} - \lambda_{665}))]$						Not applicable			[53]
	Intercept	−147.7	25.3	−220	−86.2					
	coefficient	−474.6	53.9	−607.5	−341.3					
14	**NDCI: $(SR_{708} - SR_{665})/(SR_{708} + SR_{665})$**									[54]
	Intercept	19.3	11	−17.7	39.5	99.1	8.7	79.1	121.5	
	coefficient	379.2	49.6	266.5	517.2	329.3	56.5	205.8	502.3	
15	BNDVI: $(N - B)/(N + B)$						Not applicable			[55]
	Intercept	84.8	12.6	50.2	117.9					
	coefficient	513.6	97.3	265.7	797.7					

Table A1. *Cont.*

Code	Model Algorithm	Nano-Hyperspec				Parrot Sequoia *				Ref.
		Est.	Std. e.	Min.	Max.	Est.	Std. e.	Min.	Max.	
16	INDEX: $(SR_{665}^{-1} - SR_{708}^{-1})/(SR_{753}^{-1} + SR_{708}^{-1})$						Not applicable			[56]
	Intercept	51.9	12.1	22.1	84.1					
	coefficient	79.4	20.2	44.5	139.2					
17	SABI: (N − R)/(B + G)						Not applicable			[57]
	Intercept	122.9	13.1	90.1	156.5					
	coefficient	435.3	82.6	248.1	659.6					
18	NDVI: (N − R)/(N + R)									[58]
	Intercept	125	13.7	93.2	159.6					
	coefficient	314.9	64.2	170.4	506.8					
19	AI: $((SR_{850} - SR_{660})/(SR_{850} + SR_{660})) + ((SR_{850} - SR_{625})/(SR_{850} + SR_{625}))$						Not applicable			[59]
	Intercept	180.1	22.3	120.6	231.9					
	coefficient	169.9	38.6	75.9	273.7					
20	GNDVI: (N − G)/(N + G)									[14]
	Intercept	236.8	44.4	126.7	365.2	195.1	29.0	115.6	259.7	
	coefficient	375.4	124.3	105	792.9	336.2	95.8	84.0	584.4	
21	NGRDVI: (G − R)/(G + R)									[60]
	Intercept	−18.2	39.5	−124.2	149.3	−45.6	50.8	−201.5	92.7	
	coefficient	448.5	126.2	−17.5	780	562.0	180.1	182.0	1128.5	
22	KIVU: (B − R)/G						Not applicable			[61]
	Intercept	144.6	24.7	87.7	227.3					
	coefficient	290.5	140.2	−99.7	805.7					
23	GLI: (2 × G − R − B)/(2 × G + R + B)						Not applicable			[62]
	Intercept	19.1	50.5	−100.4	177					
	coefficient	177.8	81.7	−51.1	451					
24	NGDBI: (G − B)/(G + B)						Not applicable			[63]
	Intercept	37.2	91.2	−226.6	266.1					
	coefficient	206.1	220.5	−386.8	826.5					
25	EXG: 2 × G − R − B						Not applicable			[64]
	Intercept	96.3	51.9	−22.6	249.7					
	coefficient	5915.4	14,524	−43.145	411,666					
	Semi-analytical models									
26	$[35.7 \times (SR_{708}/SR_{665}) - 19.3]^{1.124}$						Not applicable			[62]
	Intercept	−42.7	13.2	−80.7	−9.1					
	coefficient	2.7	0.3	1.9	3.4					
27	$(SR_{662} - SR_{693})/(SR_{740} + SR_{705})$						Not applicable			[63]
	Intercept	93.8	19.4	48.6	151.3					
	coefficient	212.6	109.5	41.4	491.5					

* Adapted for Sequoia bands. Code: Model Algorithm code. Est.: estimated intercept and coefficient values. Std. e.: Standard error of the intercept and coefficient values. Min.: minimum values of the intercept and coefficient values. Max.: Maximum values of the intercept and coefficient values. Ref.: Model Algorithm reference.

Table A2. More detailed statistical results of the cyanobacteria bio-optical models.

Code	Model Algorithm	Nano-Hyperspec				Parrot Sequoia				Ref.
		Est.	Std. e.	Min.	Max.	Est.	Std. e.	Min.	Max.	
	Two-band models									
28	SR_{708}/SR_{622}						Not applicable			[52]
	a	117.5	28.0	32.3	206.0					
	b	−238	71.9	−475.2	−41.5					
	c	121.3	43.2	6.8	264.6					

Table A2. *Cont.*

Code	Model Algorithm	Nano-Hyperspec				Parrot Sequoia				Ref.
		Est.	Std. e.	Min.	Max.	Est.	Std. e.	Min.	Max.	
29	SR_{710}/SR_{620}						Not applicable			[20]
	a	94.4	24.8	15.0	183.4					
	b	−196.4	65.5	−424.4	−10.0					
	c	102.0	40.0	−3.0	250.0					
30	SR_{709}/SR_{600}						Not applicable			[11]
	a	174.1	44.9	30.2	306.8					
	b	−305.8	98.3	−628.6	−20.5					
	c	134.0	50.9	0.98	310.7					
31	SR_{700}/SR_{600}						Not applicable			[66]
	a	898.5	343.4	336.9	1959.2					
	b	−1417.3	600.1	−3316.4	−404.0					
	c	558.8	259.5	99.4	1405.0					
32	SR_{724}/SR_{600}						Not applicable			[12]
	a	116.2	54.8	−41.3	279.1					
	b	−149.3	100.7	−472.5	121.9					
	c	49.3	40.9	−59.9	186.5					
33	SR_{650}/SR_{625}						Not applicable			[67]
	a	2074.7	1613.7	−7440.6	7712.1					
	b	−3691.7	3043.5	−14,563	13,896					
	c	1644.3	1434.0	−6468.2	6877.4					
34	SR_{724}/SR_{660}									[68]
	Intercept	−16.6	52.5	−168.3	150.1	−23.8	17.6	−72.9	7.6	
	coefficient *	18.2	45.5	−78.8	188.3	38.0	18.0	10.1	88.6	
	coefficient	9.0	103.3	−341.4	267.7					
	Three-band NIR and Red models									
35	$\mathbf{(SR_{624}{}^{-1} - SR_{600}{}^{-1}) \times SR_{725}}$						Not applicable			[69]
	a	1007.3	248.8	67.8	1480.0					
	b	−199.3	97.7	−424.7	94.5					
	c	11.1	6.4	−5.8	−31.9					
36	$(1/SR_{622} - 1/SR_{708}) \times SR_{755}$									[52]
	a	316.3	115.7	−64.7	640.0	34.9	19.4	8.6	90.3	
	b	−15.3	48.8	−176.6	95.2					
	c	1.6	1.9	−3.9	6.4	15.0	5.7	3.7	31.1	

Table A2. *Cont.*

Code	Model Algorithm	Nano-Hyperspec				Parrot Sequoia				Ref.
		Est.	Std. e.	Min.	Max.	Est.	Std. e.	Min.	Max.	
37	$(SR_{615}{}^{-1} - SR_{600}{}^{-1}) \times SR_{725}$						Not applicable			[70]
	a	4108.8	1122.7	5.6	6832.1					
	b	−705.9	283.2	−1540.5	171.9					
	c	29.8	14.5	−6.5	78.0					
	Index models									
38	PCI: $SR_{555} - (SR_{555} - SR_{665})/(\lambda_{655} - \lambda_{555}) \times (\lambda_{630} - \lambda_{555}) - SR_{630}$						Not applicable			[71]
	a	2.2×10^{16}	1.1×10^{16}	-1.5×10^{16}	5.4×10^{15}					
	b	90.5	27.2	36.6	159.9					
	c	10.4	4.2	1.7	22.9					
39	SLH: $SR_{714} - [SR_{654} + ((SR_{754} - SR_{654})/(\lambda_{754} - \lambda_{654})) \times (\lambda_{714} - \lambda_{654})]$						Not applicable			[72]
	a	1.4×10^{16}	1.9×10^{16}	-1.9×10^{16}	9.6×10^{15}					
	b	−4984.5	46.9	−194.1	98.6					
	c	0.16	24.1	−65.9	99.2					
40	CI: $SR_{681} - SR_{665} - (SR_{709} - SR_{665}) \times ((\lambda_{681} - \lambda_{665}))/(\lambda_{709} - \lambda_{665}))$						Not applicable			[72]
	a	2.77×10^{15}	4.73×10^{15}	-6.87×10^{15}	2.17×10^{16}					
	b	−13,755.4	59,481	−161,755	179,961					
	c	−1.1	12.5	−39.1	33.5					
41	$(SR_{556} - SR_{510})/(\lambda_{556} - \lambda_{510})$						Not applicable			[73]
	a	239.4	1850.6	−7550.6	4976.9					
	b	531.7	2266.3	−8860.5	6515.2					
	c	253.2	689.0	−2551.5	2139.5					

* Adapted for Sequoia bands. Code: Model Algorithm code. a: coefficient "a" of the second-degree term in a polynomial equation. b: coefficient "b" of the second-degree term in a polynomial equation. c: intercept "c" of the second-degree term in a polynomial equation Est.: estimated intercept and coefficient values. Std. e.: Standard error of the intercept and coefficient values. Min.: minimum values of the intercept and coefficient values. Max.: Maximum values of the intercept and coefficient values. Ref.: Model Algorithm reference.

References

1. Field, C.B.; Behrenfeld, M.J.; Randerson, J.T.; Falkowski, P. Primary Production of the Biosphere: Integrating Terrestrial and Oceanic Components. *Science* **1998**, *281*, 237–240. [CrossRef]
2. Matthews, M.W. Bio-Optical Modeling of Phytoplanton Chla. In *Bio-optical Modeling and Remote Sensing of Inland Waters*; Elsevier Inc.: Amsterdam, The Netherlands, 2017; ISBN 97801280465482017.

3. Codd, G.A. Cyanobacterial Toxins, the Perception of Water Quality, and the Prioritisation of Eutrophication Control. *Ecol. Eng.* **2000**, *16*, 51–60. [CrossRef]
4. Matthews, M.W. A Current Review of Empirical Procedures of Remote Sensing in Inland and Near-Coastal Transitional Waters. *Int. J. Remote Sens.* **2011**, *32*, 6855–6899. [CrossRef]
5. Odermatt, D.; Gitelson, A.; Brando, V.E.; Schaepman, M. Review of Constituent Retrieval in Optically Deep and Complex Waters from Satellite Imagery. *Remote Sens. Environ.* **2012**, *118*, 116–126. [CrossRef]
6. Gholizadeh, M.H.; Melesse, A.M.; Reddi, L. A Comprehensive Review on Water Quality Parameters Estimation Using Remote Sensing Techniques. *Sensors* **2016**, *16*, 1298. [CrossRef] [PubMed]
7. Dörnhöfer, K.; Oppelt, N. Remote Sensing for Lake Research and Monitoring—Recent Advances. *Ecol. Indic.* **2016**, *64*, 105–122. [CrossRef]
8. Ogashawara, I.; Mishra, D.R.; Gitelson, A.A. Remote Sensing of Inland Waters: Background and Current State-of-the-Art. In *Bio-optical Modeling and Remote Sensing of Inland Waters*; Elsevier Inc.: Amsterdam, The Netherlands, 2017; ISBN 97801280465482017.
9. Li, L.; Song, K. Bio-Optical Modeling of Phycocyanin. In *Bio-optical Modeling and Remote Sensing of Inland Waters*; Elsevier Inc.: Amsterdam, The Netherlands, 2017; ISBN 97801280465482017.
10. Olmanson, L.G.; Brezonik, P.L.; Bauer, M.E. Remote Sensing for Regional Lake Water Quality Assessment: Capabilities and Limitations of Current and Upcoming Satellite Systems. *Adv. Watershed Sci. Assess. Handb. Environ. Chem.* **2015**, *33*, 111–140. [CrossRef]
11. Morel, A.; Prieur, L. Analysis of Variations in Ocean Color. *Limnol. Oceanogr.* **1977**, *22*, 709–722. [CrossRef]
12. Gitelson, A.A.; Yacobi, Y.Z.; Rundquist, D.C.; Stark, R.; Han, L.; Etzion, D. Remote Estimation of Chlorophyll Concentration in Productive Waters: Principals, Algorithm Development and Validation. In Proceedings of the NWQMC National Monitoring Conference 2000, Austin, TX, USA, 25–27 April 2000; pp. 149–160.
13. Neil, C.; Spyrakos, E.; Hunter, P.D.; Tyler, A.N. A Global Approach for Chlorophyll-a Retrieval across Optically Complex Inland Waters Based on Optical Water Types. *Remote Sens. Environ.* **2019**, *229*, 159–178. [CrossRef]
14. Mishra, S.; Mishra, D.R.; Lee, Z.; Tucker, C.S. Quantifying Cyanobacterial Phycocyanin Concentration in Turbid Productive Waters: A Quasi-Analytical Approach. *Remote Sens. Environ.* **2013**, *133*, 141–151. [CrossRef]
15. Ogashawara, I.; Mishra, D.R.; Mishra, S.; Curtarelli, M.P.; Stech, J.L. A Performance Review of Reflectance Based Algorithms for Predicting Phycocyanin Concentrations in Inland Waters. *Remote Sens.* **2013**, *5*, 4774–4798. [CrossRef]
16. Yao, H.; Qin, R.; Chen, X. Unmanned Aerial Vehicle for Remote Sensing Applications—A Review. *Remote Sens.* **2019**, *11*, 1443. [CrossRef]
17. Kislik, C.; Dronova, I.; Kelly, M. UAVs in Support of Algal Bloom Research: A Review of Current Applications and Future Opportunities. *Drones* **2018**, *2*, 35. [CrossRef]
18. Koutalakis, P.; Tzoraki, O. UAVs for Hydrologic Scopes: Application of a Low-Cost UAV to Estimate Surface Water Velocity by Using Three Different Image-Based Methods. *Drones* **2019**, *3*, 14. [CrossRef]
19. Koutalakis, P.; Tzoraki, O.; Gkiatas, G.; Zaimes, G.N. Using UAV to capture and record torrent bed and banks, flood debris, and riparian areas. *Drones* **2020**, *4*, 77. [CrossRef]
20. Zhu, W.; Yu, Q.; Tian, Y.Q.; Chen, R.F.; Gardner, G.B. Estimation of Chromophoric Dissolved Organic Matter in the Mississippi and Atchafalaya River Plume Regions Using above—Surface Hyperspectral Remote Sensing. *J. Geophys. Res. Ocean.* **2011**, *116*, 1–22. [CrossRef]
21. Dronova, I.; Kislik, C.; Dinh, Z.; Kelly, M. A Review of Unoccupied Aerial Vehicle Use in Wetland Applications: Emerging Opportunities in Approach, Technology, and Data. *Drones* **2021**, *5*, 45. [CrossRef]
22. Tóth, V.Z.; Grósz, J.; Ladányi, M.; Jung, A. A New Lake Algae Detection Method Supported by a Drone-Based Multispectral Camera. *Lakes Reserv. Res. Manag.* **2021**, *26*, 1–8. [CrossRef]
23. Lee, H.; Kang, T.; Pyo, J.; Park, Y.; Kwon, Y.; Cho, S.; Cho, K.; Ahn, M.-H.; Ligaray, M.; Kim, K. High-Spatial Resolution Monitoring of Phycocyanin and Chlorophyll-a Using Airborne Hyperspectral Imagery. *Remote Sens.* **2018**, *10*, 1180. [CrossRef]
24. Kwon, Y.S.; Pyo, J.C.; Kwon, Y.H.; Duan, H.; Cho, K.H.; Park, Y. Drone-Based Hyperspectral Remote Sensing of Cyanobacteria Using Vertical Cumulative Pigment Concentration in a Deep Reservoir. *Remote Sens. Environ.* **2020**, *236*, 111517. [CrossRef]
25. Cui, M.; Sun, Y.; Huang, C.; Li, M. Water Turbidity Retrieval Based on UAV Hyperspectral Remote Sensing. *Water* **2022**, *14*, 128. [CrossRef]
26. Olivetti, D.; Roig, H.; Martinez, J.; Borges, H. Low-Cost Unmanned Aerial Multispectral Imagery for Siltation Monitoring in Reservoirs. *Remote Sens.* **2020**, *12*, 1855. [CrossRef]
27. Kwon, S.; Seo, I.W.; Noh, H.; Kim, B. Hyperspectral Retrievals of Suspended Sediment Using Cluster-Based Machine Learning Regression in Shallow Waters. *Sci. Total Environ.* **2022**, *833*, 155168. [CrossRef] [PubMed]
28. Windle, A.E.; Silsbe, G.M.; Moses, W. Evaluation of Unoccupied Aircraft System (UAS) Remote Sensing Re Fl Ectance Retrievals for Water Quality Monitoring in Coastal Waters. *Front. Environ. Sci.* **2021**, *9*, 674247. [CrossRef]
29. Román, A.; Tovar-s, A.; Gauci, A.; Deidun, A.; Caballero, I.; Colica, E.; Amico, S.D.; Navarro, G. Water-Quality Monitoring with a UAV-Mounted Multispectral Camera in Coastal Waters. *Remote Sens.* **2023**, *15*, 237. [CrossRef]
30. Aasen, H.; Honkavaara, E.; Lucieer, A.; Zarco-Tejada, P.J. Quantitative Remote Sensing at Ultra-High Resolution with UAV Spectroscopy: A Review of Sensor Technology, Measurement Procedures, and Data Correctionworkflows. *Remote Sens.* **2018**, *10*, 1091. [CrossRef]

31. APHA—Association American Public Health. *Standard Methods for the Examination of Water and Wastewater*, 22nd ed.; APHA, WWA, WPCR, Eds.; APHA: Washington, DC, USA, 2012.
32. Wójcik, K.A.; Bialik, R.J.; Osińska, M.; Figielski, M. Investigation of Sediment-Rich Glacial Meltwater Plumes Using a High-Resolution Multispectral Sensor Mounted on an Unmanned Aerial Vehicle. *Water* **2019**, *11*, 2405. [CrossRef]
33. Westoby, M.J.; Brasington, J.; Glasser, N.F.; Hambrey, M.J.; Reynolds, J.M. Structure-from-Motion'photogrammetry: A low-cost, effective tool forgeoscience applications. *Geomorphology* **2012**, *179*, 14. [CrossRef]
34. Vydhyanathan, A.; Bellusci, G. XSens Mti-G White Paper: The Next Generation Xsens Motion Trackers for Industrial Applications. XSENS, version 2.0.5. 2018, pp. 1–10. Available online: https://www.xsens.com/hubfs/Downloads/Whitepapers/MTi_whitepaper.pdf (accessed on 2 April 2023).
35. Wei, L.; Huang, C.; Zhong, Y.; Wang, Z.; Hu, X.; Lin, L. Inland Waters Suspended Solids Concentration Retrieval Based on PSO-LSSVM for UAV-Borne Hyperspectral Remote Sensing Imagery. *Remote Sens.* **2019**, *11*, 1455. [CrossRef]
36. Overstreet, B.T.; Legleiter, C.J. Removing Sun Glint from Optical Remote Sensing Images of Shallow Rivers. *Earth Surf. Process. Landforms* **2017**, *42*, 318–333. [CrossRef]
37. Zeng, C.; Richardson, M.; King, D.J. The Impacts of Environmental Variables on Water Reflectance Measured Using a Lightweight Unmanned Aerial Vehicle (UAV)-Based Spectrometer System. *ISPRS J. Photogramm. Remote Sens.* **2017**, *130*, 217–230. [CrossRef]
38. Mobley, C.D. Estimation of the Remote-Sensing Reflectance from above-Surface Measurements. *Appl. Opt.* **1999**, *38*, 7442–7455. [CrossRef]
39. Bracewell, R. The Fourier Transform. *Sci. Am.* **1989**, *260*, 86–95. [CrossRef]
40. Ogashawara, I. Terminology and Classification of Bio-Optical Algorithms. *Remote Sens. Lett.* **2015**, *6*, 613–617. [CrossRef]
41. Ansper, A.; Alikas, K. Retrieval of Chlorophyll a from Sentinel-2 MSI Data for the European Union Water Framework Directive Reporting Purposes. *Remote Sens.* **2019**, *11*, 64. [CrossRef]
42. Statistics, M. Bootstrap Methods: Another Look at the Jackknife. *Statistics* **2008**, *7*, 1–26.
43. Kulesa, A.; Krzywinski, M.; Blainey, P.; Altman, N. Sampling Distributions and the Bootstrap: The Bootstrap Can Be Used to Assess Uncertainty of Sample Estimates. *Nat. Methods* **2015**, *12*, 477–478. [CrossRef]
44. Ministério Do Meio Ambiente, Conselho Nacional Do Meio Ambiente Resolução Nº 430, DE 13 DE MAIO DE 2011. Available online: https://anmlegis.datalegis.inf.br/action/ActionDatalegis.php?acao=abrirTextoAto&link=S&tipo=RES&numeroAto=00000430&seqAto=000&valorAno=2011&orgao=CONAMA/MMA&cod_modulo=405&cod_menu=6783 (accessed on 13 May 2021).
45. Moses, W.J.; Sterckx, S.; Montes, M.J.; De Keukelaere, L.; Knaeps, E. Atmospheric Correction for Inland Waters. In *Bio-optical Modeling and Remote Sensing of Inland Waters*; Elsevier Inc.: Amsterdam, The Netherlands, 2017; ISBN 97801280465482017.
46. Kirk, J.T.O. *Light and Photosynthesis in Aquatic Ecosystems*, 3rd ed.; Kirk, J.T.O., Ed.; University Press: Cambridge, UK, 2011.
47. Dekker, A.G. Detection of Optical Water Quality Parameters for Eutrophic Waters by High Resolution Remote Sensing. Ph.D. Thesis, Vrije Universiteit Amsterdam, Amsterdam, The Netherlands, 1993; p. 222.
48. Cicerelli, R.E.; Galo, M.D.L.B.T.; Roig, H.L. Multisource Data for Seasonal Variability Analysis of Cyanobacteria in a Tropical Inland Aquatic Environment. *Mar. Freshw. Res.* **2017**, *68*, 2344–2354. [CrossRef]
49. Yan, Y.; Bao, Z.; Shao, J. Phycocyanin Concentration Retrieval in Inland Waters: A Comparative Review of the Remote Sensing Techniques and Algorithms. *J. Great Lakes Res.* **2018**, *44*, 748–755. [CrossRef]
50. Moses, W.J.; Gitelson, A.A.; Berdnikov, S.; Povazhnyy, V. Satellite Estimation of Chlorophyll-a Concentration Using the Red and NIR Bands of MERISThe Azov Sea Case Study. *IEEE Geosci. Remote Sens. Lett.* **2009**, *6*, 845–849. [CrossRef]
51. Gitelson, A.A.; Gurlin, D.; Moses, W.J.; Barrow, T. A Bio-Optical Algorithm for the Remote Estimation of the Chlorophyll-a Concentration in Case 2 Waters. *Environ. Res. Lett.* **2009**, *4*, 2–7. [CrossRef]
52. Moses, W.J.; Gitelson, A.A.; Perk, R.L.; Gurlin, D.; Rundquist, D.C.; Leavitt, B.C.; Barrow, T.M.; Brakhage, P. Estimation of Chlorophyll- a Concentration in Turbid Productive Waters Using Airborne Hyperspectral Data. *Water Res.* **2011**, *46*, 993–1004. [CrossRef] [PubMed]
53. Zhang, Y.; Ma, R.; Duan, H.; Loiselle, S.; Xu, J. A Spectral Decomposition Algorithm for Estimating Chlorophyll-a Concentrations in Lake Taihu, China. *Remote Sens.* **2014**, *6*, 5090–5106. [CrossRef]
54. Gitelson, A.A.; Gritz, Y.; Merzlyak, M.N. Relationships between Leaf Chlorophyll Content and Spectral Reflectance and Algorithms for Non-Destructive Chlorophyll Assessment in Higher Plant Leaves. *J. Plant Physiol.* **2003**, *160*, 271–282. [CrossRef] [PubMed]
55. Moses, W.J.; Gitelson, A.A.; Berdnikov, S.; Povazhnyy, V. Estimation of Chlorophyll- *a* Concentration in Case II Waters Using MODIS and MERIS Data—Successes and Challenges. *Environ. Res. Lett.* **2009**, *4*, 045005. [CrossRef]
56. Gower, J.; King, S.; Borstad, G.; Brown, L. Detection of Intense Plankton Blooms Using the 709 Nm Band of the MERIS Imaging Spectrometer. *Int. J. Remote Sens.* **2005**, *26*, 2005–2012. [CrossRef]
57. Mishra, S.; Mishra, D.R. Normalized Difference Chlorophyll Index: A Novel Model for Remote Estimation of Chlorophyll-a Concentration in Turbid Productive Waters. *Remote Sens. Environ.* **2012**, *117*, 394–406. [CrossRef]
58. Van der Merwe, D.; Price, K.P. Harmful Algal Bloom Characterization at Ultra-High Spatial and Temporal Resolution Using Small Unmanned Aircraft Systems. *Toxins* **2015**, *7*, 1065–1078. [CrossRef]

59. Yang, W.; Matsushita, B.; Chen, J.; Fukushima, T.; Ma, R. An Enhanced Three-Band Index for Estimating Chlorophyll-a in Turbid Case-II Waters: Case Studies of Lake Kasumigaura, Japan, and Lake Dianchi, China. *IEEE Geosci. Remote Sens. Lett.* **2010**, *7*, 655–659. [CrossRef]
60. Alawadi, F. Detection of Surface Algal Blooms Using the Newly Developed Algorithm Surface Algal Bloom Index (SABI). *Remote Sens. Ocean. Sea Ice Large Water Reg.* **2010**, *7825*, 782506. [CrossRef]
61. Rouse, J.W.J.; Haas, R.H.; Deering, D.W.; Shell, J.A.; Harlan, J.C. *Monitoring the Vernal Advancement and Retrogradation (Green Wave Effect) of Natural Vegetation*; NASA/GSFC Type III Final Report; NASA/GSFC: Greenbelt, MD, USA, 1974; p. 371.
62. Jang, S.W.; Yoon, H.J.; Kwak, S.N.; Sohn, B.Y.; Kim, S.G.; Kim, D.H. Algal Bloom Monitoring Using UAVs Imagery. *Adv. Sci. Technol. Lett.* **2016**, *138*, 30–33. [CrossRef]
63. Xu, F.; Gao, Z.; Jiang, X.; Shang, W.; Ning, J.; Song, D.; Ai, J. A UAV and S2A Data-Based Estimation of the Initial Biomass of Green Algae in the South Yellow Sea. *Mar. Pollut. Bull.* **2018**, *128*, 408–414. [CrossRef]
64. Brivio, P.A.; Giardino, C.; Zilioli, E. Determination of Chlorophyll Concentration Changes in Lake Garda Using an Image-Based Radiative Transfer Code for Landsat TM Images. *Int. J. Remote Sens.* **2001**, *22*, 487–502. [CrossRef]
65. Gilerson, A.; Zhou, J.; Hlaing, S.; Ioannou, I.; Gross, B.; Moshary, F.; Ahmed, S. Fluorescence Component in the Reflectance Spectra from Coastal Waters. II. Performance of Retrieval Algorithms. *Opt. Express* **2008**, *16*, 2446. [CrossRef] [PubMed]
66. Le, C.; Li, Y.; Zha, Y.; Sun, D.; Huang, C.; Lu, H. A Four-Band Semi-Analytical Model for Estimating Chlorophyll a in Highly Turbid Lakes: The Case of Taihu Lake, China. *Remote Sens. Environ.* **2009**, *113*, 1175–1182. [CrossRef]
67. Matthews, M.W.; Bernard, S.; Evers-King, H.; Robertson Lain, L. Distinguishing Cyanobacteria from Algae in Optically Complex Inland Waters Using a Hyperspectral Radiative Transfer Inversion Algorithm. *Remote Sens. Environ.* **2020**, *248*, 111981. [CrossRef]
68. Mishra, S.; Stumpf, R.P.; Schaeffer, B.A.; Werdell, P.J.; Loftin, K.A.; Meredith, A. Measurement of Cyanobacterial Bloom Magnitude Using Satellite Remote Sensing. *Sci. Rep.* **2019**, *9*, 18310. [CrossRef]
69. Simis, S.G.H.; Ruiz-Verdú, A.; Domínguez-Gómez, J.A.; Peña-Martinez, R.; Peters, S.W.M.; Gons, H.J. Influence of Phytoplankton Pigment Composition on Remote Sensing of Cyanobacterial Biomass. *Remote Sens. Environ.* **2007**, *106*, 414–427. [CrossRef]
70. Mishra, S.; Mishra, D.R.; Schluchter, W.M. A Novel Algorithm for Predicting Phycocyanin Concentrations in Cyanobacteria: A Proximal Hyperspectral Remote Sensing Approach. *Remote Sens.* **2009**, *1*, 758–775. [CrossRef]
71. Schalles, J.F.; Yacobi, Y.Z. Remote Detection and Seasonal Patterns of Phycocyanin, Carotenoid and Chlorophyll Pigments in Eutrophic Waters. *Ergeb. Limnol.* **2000**, *55*, 153–168.
72. Woźniak, M.; Bradtke, K.M.; Darecki, M.; Kręzel, A. Empirical Model for Phycocyanin Concentration Estimation as an Indicator of Cyanobacterial Bloom in the Optically Complex Coastalwaters of the Baltic Sea. *Remote Sens.* **2016**, *8*, 212. [CrossRef]
73. Li, L.; Li, L.; Shi, K.; Li, Z.; Song, K. A Semi-Analytical Algorithm for Remote Estimation of Phycocyanin in Inland Waters. *Sci. Total Environ.* **2012**, *435–436*, 141–150. [CrossRef]
74. Hunter, P.D.; Tyler, A.N.; Présing, M.; Kovács, A.W.; Preston, T. Spectral Discrimination of Phytoplankton Colour Groups: The Effect of Suspended Particulate Matter and Sensor Spectral Resolution. *Remote Sens. Environ.* **2008**, *112*, 1527–1544. [CrossRef]
75. Qi, L.; Hu, C.; Duan, H.; Cannizzaro, J.; Ma, R. A Novel MERIS Algorithm to Derive Cyanobacterial Phycocyanin Pigment Concentrations in a Eutrophic Lake: Theoretical Basis and Practical Considerations. *Remote Sens. Environ.* **2014**, *154*, 298–317. [CrossRef]
76. Kudela, R.M.; Palacios, S.L.; Austerberry, D.C.; Accorsi, E.K.; Guild, L.S.; Torres-Perez, J. Application of Hyperspectral Remote Sensing to Cyanobacterial Blooms in Inland Waters. *Remote Sens. Environ.* **2015**, *167*, 196–205. [CrossRef]
77. Dash, P.; Walker, N.D.; Mishra, D.R.; Hu, C.; Pinckney, J.L.; D'Sa, E.J. Estimation of Cyanobacterial Pigments in a Freshwater Lake Using OCM Satellite Data. *Remote Sens. Environ.* **2011**, *115*, 3409–3423. [CrossRef]
78. Gitelson, A. The Peak near 700 Nm on Radiance Spectra of Algae and Water: Relationships of Its Magnitude and Position with Chlorophyll concentration. *Int. J. Remote Sens.* **1992**, *13*, 3367–3373. [CrossRef]
79. Jiang, G.; Loiselle, S.A.; Yang, D.; Ma, R.; Su, W.; Gao, C. Remote Estimation of Chlorophyll a Concentrations over a Wide Range of Optical Conditions Based on Water Classification from VIIRS Observations. *Remote Sens. Environ.* **2020**, *241*, 111735. [CrossRef]
80. Tavares, M.H.; Lins, R.C.; Harmel, T.; Fragoso, C.R., Jr.; Martínez, J.-M.; Motta-Marques, D. Atmospheric and Sunglint Correction for Retrieving Chlorophyll-a in a Productive Tropical Estuarine-Lagoon System Using Sentinel-2 MSI Imagery. *ISPRS J. Photogramm. Remote Sens.* **2021**, *174*, 215–236. [CrossRef]
81. Castro, C.C.; Antonio, J.; Delgado, J.; Alejandro, B.; Hinojo, S.; Luis, J.; Arango, C.; Andr, F.; Tuya, C.; Ramon, D. An UAV and Satellite Multispectral Data Approach to Monitor Water Quality in Small Reservoirs. *Remote Sens.* **2020**, *12*, 1514. [CrossRef]
82. Salem, S.I.; Higa, H.; Kim, H.; Kobayashi, H.; Oki, K.; Oki, T. Assessment of Chlorophyll-a Algorithms Considering Different Trophic Statuses and Optimal Bands. *Sensors* **2017**, *17*, 1746. [CrossRef] [PubMed]
83. Zhang, D.; Lavender, S.; Muller, J.P.; Walton, D.; Karlson, B.; Kronsell, J. Determination of Phytoplankton Abundances (Chlorophyll-a) in the Optically Complex Inland Water—The Baltic Sea. *Sci. Total Environ.* **2017**, *601–602*, 1060–1074. [CrossRef] [PubMed]
84. Huang, C.; Zou, J.; Li, Y.; Yang, H.; Shi, K.; Li, J.; Wang, Y.; Chena, X.; Zheng, F. Assessment of NIR-Red Algorithms for Observation of Chlorophyll-a in Highly Turbid Inland Waters in China. *ISPRS J. Photogramm. Remote Sens.* **2014**, *93*, 29–39. [CrossRef]
85. Chen, J.; Zhu, W.; Tian, Y.Q.; Yu, Q.; Zheng, Y.; Huang, L. Remote Estimation of Colored Dissolved Organic Matter and Chlorophyll-a in Lake Huron Using Sentinel-2 Measurements. *J. Appl. Remote Sens.* **2017**, *11*, 1. [CrossRef]

86. Lins, R.C.; Martinez, J.M.; da Motta Marques, D.; Cirilo, J.A.; Fragoso, C.R. Assessment of Chlorophyll-a Remote Sensing Algorithms in a Productive Tropical Estuarine-Lagoon System. *Remote Sens.* **2017**, *9*, 516. [CrossRef]
87. Watanabe, F.; Alcântara, E.; Rodrigues, T.; Rotta, L.; Bernardo, N.; Imai, N. Remote Sensing of the Chlorophyll-a Based on OLI/Landsat-8 and MSI/Sentinel-2a (Barra Bonita Reservoir, Brazil). *An. Acad. Bras. Cienc.* **2018**, *90*, 1987–2000. [CrossRef]
88. Zhou, X.; Liu, C.; Akbar, A.; Xue, Y.; Zhou, Y. Spectral and Spatial Feature Integrated Ensemble Learning Method for Grading Urban River Network Water Quality. *Remote Sens.* **2021**, *13*, 4591. [CrossRef]
89. Stumpf, R.P.; Davis, T.W.; Wynne, T.T.; Graham, J.L.; Loftin, K.A.; Johengen, T.H.; Gossiaux, D.; Palladino, D.; Burtner, A. Challenges for Mapping Cyanotoxin Patterns from Remote Sensing of Cyanobacteria. *Harmful Algae* **2016**, *54*, 160–173. [CrossRef]
90. Klemas, V. Remote Sensing of Algal Blooms: An Overview with Case Studies. *J. Coast. Res.* **2012**, *278*, 34–43. [CrossRef]
91. Ruiz-Verdú, A.; Simis, S.G.H.; de Hoyos, C.; Gons, H.J.; Peña-Martínez, R. An Evaluation of Algorithms for the Remote Sensing of Cyanobacterial Biomass. *Remote Sens. Environ.* **2008**, *112*, 3996–4008. [CrossRef]